Scholars' Mine

Fall 2007

Development, modeling, and simulation of a nano aerial vehicle using empirical data

Wyatt Emery Davenport

DEVELOPMENT, MODELING, AND SIMULATION OF A NANO AERIAL

VEHICLE USING EMPIRICAL DATA

by

WYATT EMERY DAVENPORT

A THESIS

Presented to the Faculty of the Graduate School of the

UNIVERSITY OF MISSOURI-ROLLA

In Partial Fulfillment of the Requirements for the Degree

MASTER OF SCIENCE IN MECHANICAL ENGINEERING

2007

Approved by

_____   _____
Dr. D. McAdams, Advisor   **Dr. R. Landers, Co-Advisor**

_____
Dr. K. M. Isaac

ABSTRACT

The ultimate goals of this study were to use experimental data to estimate the flight capabilities of a flapping wing nano aerial vehicle (NAV), estimate the power required to provide such flight, and develop a controller approach for future use in the design of this aircraft. The experimental data is a collection of measurements of the normal force on a flapping wing taken in stationary water, and was used to develop empirical coefficient derivatives for use in the dynamic modeling of the NAV. The mathematical modeling of this aircraft was undertaken from a predominantly mechanical point-of-view; that is to say the knowledge of more complex aerodynamic concepts, such as the unsteady effects that arise with flapping and pitching wings, was limited. This did not inhibit the design process in the study however, since the empirical coefficients should account for all of the underlying unsteady effects in flapping flight.

Using the empirical coefficients, the aircraft was designed using stability techniques. However, current stability concepts in aircraft design are limited to the fixed wing aircraft field. Therefore, a laterally stable aircraft on the micro aerial vehicle (MAV) scale was developed to acquaint the designer with rudimentary aircraft design, and once the dynamic model was deemed appropriate for the fixed wing aircraft, the design technique was applied to a flapping wing NAV. With the ensuing two-dimensional dynamic model, simulations were developed to obtain power requirements. Finally, a three-dimensional tailless NAV was designed for further simulations and testing, and several controller schemes were developed for the two-dimensional flapping wing NAV.

ACKNOWLEDGEMENTS

I would like to extend my wholehearted appreciation to my advisor Dr. Daniel McAdams, for the opportunity to further my education and intellectual development with such an intriguing and exhausting project. Not only did Dr. McAdams serve the role of advisor on topics related to campus and this project, but also as a valuable source of insight and advice in the non-collegiate matters of daily life.

I would also like to extend similar thanks to my co-advisor Dr. Robert Landers, and committee member Dr. K. M. Isaac. Both of these men, and in fact most of the Mechanical Engineering faculty, exemplified the meaning of the open-door policy, admitting me at every knock on the door to offer much needed advice, ideas, and critique.

Genuine thanks are also due for the NASA-Missouri Space Grant Consortium, which not only awarded a much needed fellowship for expenses arising during the course of this research, but also for the opportunity to gather and present a portion of my work to a group of the aerospace community.

I would like to thank Jason Searcy and Michael Dancer for their help. And to my family; I would like to thank my wife Laura for supporting me these past five years; giving encouragement from 250 miles away for the first three of those years, and providing the primary income and source of motivation at our home for the last two years. All of this is for her, and for our children to come. I would not have been able to accomplish this without the continual advice, praise, and encouragement from my father and mother. To my grandparents, those still with us and passed on, you will never know how big a role you played in this. And lastly to my brothers; each one of you has set the bar high above me, which has given me the motivation to carry this through.

TABLE OF CONTENTS

LIST OF ILLUSTRATIONS

LIST OF TABLES

NOMENCLATURE

Symbol	Description
S_x	Total area of surface x ($x = w$ for wing, $x = t$ for tail) (m^2)
$S_{exp,x}$	Total exposed area for surface x (m^2)
A	Aspect ratio
λ	Tail taper ratio
Λ_{LE}	Tail leading edge sweep (rad)
$\Lambda_{c/4}$	Tail quarter chord sweep (rad)
c_w	Wing root chord length (m)
c_{rt}	Tail root chord length (m)
c_{tt}	Tail tip chord length (m)
$\bar{c}_t$	Tail mean chord length (m)
b_w	Total wingspan (m)
b_t	Total tailspan (m)
c_{ht}	Horizontal tail volume coefficient
L_t	Distance between wing and tail aerodynamic centers (m)
L_f	Length of fuselage (m)
M_{cg}	Resultant moment about the aircraft center of gravity (Nm)
L_x	Total lift at surface x (N)

X_p	Position p on the aircraft; measured from the nose of the aircraft ($p = acw$ for wing aerodynamic center, $p = act$ for tail aerodynamic center, $p = cg$ for center of gravity).
q	Dynamic pressure *(kg/ms²)*
q_t	Tail dynamic pressure *(kg/ms²)*
ρ	Fluid density *(kg/m³)*
V_∞^2	Square of ambient fluid velocity *(m²/s²)*
$C_{m_{cg}}$	Moment coefficient about the center of gravity
C_{Lx}	Lift coefficient for surface x
M	Mach number
d_x	Fuselage diameter at x
$C_{Lx\alpha}$	Coefficient of lift derivative for surface x
$C_{Dx\alpha}$	Coefficient of drag derivative for surface x
C_{D0}	Parasite drag constant
C_L	Coefficient for empirical lift coefficient derivative
C_D	Coefficient for empirical lift coefficient derivative
C_f	Coefficient derivative function
R_E^b	3-2-1 rotation matrix
$\bar{v}_I$	Inertial frame velocity vector ($\dot{x}_E, \dot{y}_E, \dot{z}_E$) *(m/s)*
$\bar{v}_b$	Body frame velocity vector (v_x, v_y, v_z) *(m/s)*
$\bar{\omega}_I$	Inertial angular velocity vector (ψ, θ, ϕ) *(rad/s)*
$\bar{\omega}_b$	Body frame angular velocity vector ($\omega_x, \omega_y, \omega_z$) *(rad/s)*
m	Aircraft mass *(kg)*
g	Gravitational constant *(9.8 m/s²)*

M_a^b	Aerodynamic moments acting on the aircraft in the body coordinates *(Nm)*
F_a^b	Aerodynamic forces acting on the aircraft in the body coordinates *(N)*
I_b	Moments of inertia of the aircraft in body coordinates *(kgm²)*
I_{xx}'	Specific principle moment of inertia *(m²)*
W_b	Aircraft weight vector in body coordinates *(N)*
α_{eq}	Equivalent angle of attack at the wing *(rad)*
α	Aircraft and tail angle of attack *(rad)*
α_t	Tail incidence angle *(rad)*
α_0	Wing pitch angle; control input *(rad)*
α_L	Left wing nominal pitch angle *(rad)*
α_R	Right wing nominal pitch angle *(rad)*
α_{set}	Wing offset pitch angle *(rad)*
α_δ	Wing variation angle *(rad)*
V_{eq}^2	Equivalent fluid velocity at the wing mean chord *(m/s)*
V_∞^2	Fluid velocity at tail *(m/s)*
V	Lyapunov function
$\dot{V}$	Lyapunov derivative
P	Required power at wings
$A(\mathbf{x})$	State dependent coefficient of system states
$B(\mathbf{x})$	State dependent coefficient of system control signal(s)
K	Gain vector for SDRE controller
S	Solution to Riccati equation for SDRE controller
eig	Eigenvalues at each time step for SDRE controller

G Gain vector for state dependent regulator

p_{1-5} User selected poles to be placed with state dependent regulator

1. INTRODUCTION

1.1. MOTIVATION

Unmanned aerial vehicles (UAV) are becoming increasingly important on the modern military and civilian scene. These aircraft allow military personnel to pursue reconnaissance objectives and deliver payloads without placing soldiers in dangerous situations, and could also be used for civilian purposes such as chemical agent detection at hazardous sites or crop dusting. As seems to be the path taken by most technology, an effort to reduce the size while maintaining a viable and useful UAV has been underway since the start of the century. The Defense Advanced Research Projects Agency (DARPA) began funding projects for the purpose of developing micro aerial vehicles (MAV), and now a push is being made for nano aerial vehicles (NAV). Neither of these vehicles is an accurate representation of the micro or nano scales, the name simply implies the size of the vehicle relative to the original UAV scale.

In order for a UAV to be considered in the class NAV, DARPA has the following requirements:

- Gross mass of 10 g (including a 2 g payload)

- No dimension larger than 7.5 cm

- Fast forward speed (FFS) of 5-10 m/s

- Slow forward speed (SFS) of 0.5 m/s

- Range greater than 1000 m at FFS

- Ability to transition from FFS to SFS after completing 1000 *m*, then maintain SFS for greater than 60 *s*, then hover for greater than 60 *s*

- Trip or hover endurance of at least 30 *min*

The significant physical differences between a MAV and a NAV are that a MAV has a maximum gross mass of 100 *g*, and a maximum dimension of 15 *cm*. Examining the desired flight capabilities presented by DARPA, it is evident that an aircraft that meets these objectives would be ideal for use in the current urban warfare environment. Depending on the complexity of the aircraft operation, it is easy to envision every squadron or platoon equipped with a NAV specialist such that this single soldier could operate the system for short range reconnaissance, chemical agent detection, or payload delivery. The ability to hover would allow a NAV with an onboard camera to enter buildings in a war zone to determine if occupants are friendly or foe, and if the latter proved to be the case, the enemy positions and strength could be determined. Like many previous technologies that began as military concepts, a capable and effective NAV would undoubtedly find civilian uses as well; a NAV could be sent down mine shafts to determine oxygen levels or one with thermal imagery capabilities could be used in search and rescue missions in hazardous or inaccessible locations.

1.2. STUDY GOALS AND APPROACH

Most previous studies of flapping wing flight revolve around understanding and defining the aerodynamic effects associated with the unsteady characteristics of a flapping wing. However, even after an adequate model or approximation is made to

account for these phenomena, the stability of the aircraft can still be in question. Aircraft stability is not only dependent on its aerodynamic characteristics like lift and drag, but also on the geometric aspects of the aircraft. Therefore, the first goal of this study was to develop a straightforward and feasible approach to design a stable flapping wing aircraft. Since most present literature on aircraft stability deals exclusively with fixed wing aircraft, the method defined in these works was applied to a flapping wing aircraft with the assumption that, in terms of stability, a flapping wing aircraft in forward flight behaves approximately the same as a fixed wing aircraft.

Following this procedure, a fixed wing aircraft corresponding to MAV size was designed first and simulated to ensure confidence in the design method. Then, using the same approach developed for the fixed wing, a flapping wing aircraft of NAV scale was developed and simulated. The fixed wing aircraft and the first flapping wing aircraft both had dummy tails, or tails with no control surfaces, to help with stability. The uncontrolled tail reduces system weight with the absence of linkages and extra moving parts, but the system was still controlled by varying the incidence angle of the fixed wing or the nominal pitch angle of the flapping wing during simulations. An effort was made at the end of this study to design a tailless aircraft to further reduce weight.

Even though the approach used to calculate the geometric parameters that define a statically stable fixed wing aircraft was also used for the flapping wing aircraft, the aerodynamic properties of the flapping wing aircraft, such as lift and drag, still needed to be defined. This was accomplished using a collection of experimental data measuring the normal force on a single flapping wing in stationary water over a single stroke. Using

this experimental data, empirical lift and drag coefficient derivatives were developed to use during simulations of both flapping wing aircraft.

Lastly, several controller design schemes were developed for future use on this project. For the flapping wing aircraft with the tail, all simulations were in a two dimensional plane, and therefore the nominal wing pitch angle was kept the same on each wing. This single wing pitch angle is used as the only system input. The dynamic system is highly nonlinear, and control schemes included methods such as feedback linearization, Lyaponuv design, two methods of optimal control of a state dependent Riccati equation, and two approaches with a state dependent regulator.

The main objective of this project was to develop an estimation of the power required for flight. With this estimation, appropriate equipment could be purchased to further the project with a working model to benchmark the simulations and controllers.

2. REVIEW OF LITERATURE

2.1. EXISTING MICRO AERIAL VEHICLES

During preliminary investigation, several existing micro aerial vehicle (MAV) projects were studied and analyzed. The purpose of this step was to develop a template of the primary MAV roadblocks and the attempted solutions of those obstructions. The models found primarily consisted of three aerodynamic types: fixed wing, flapping wing, and rotary. The *Entomopter* of Georgia Tech [1] in Figure 2.1 is a flapping wing model as are the *Microbat* [2] and the micro-mechanical flying insect, or *MFI* [3] in Figure 2.2 and Figure 2.3 respectively.

Figure 2.1. Georgia Tech's Conceptual *Entomopter*, X-wing Configuration.

The flapping wing MAV use a wing motion similar to biological flyers to achieve the aerodynamic effects of lift and thrust.

Figure 2.2. The *Microbat*.
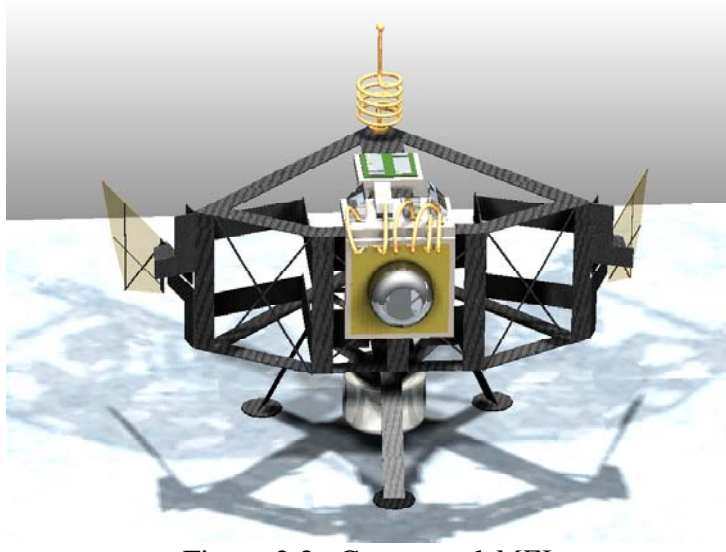
Figure 2.3. Conceptual *MFI*.

The *Black Widow* [4], *MITE* [5], *TH360* [6], *WASP* and *Hornet* [7], *MicroSTAR* and *Palmtop* [8], and the MAV developed by Notre Dame [9] and the Indian Institute of Technology at Bombay [10] are all stationary winged aircraft. For simplicity, the Notre Dame and Indian Institute of Technology's models will be referred to as *ND* and *Indian*, respectively. Notice that the *Black Widow* in Figure 2.4 and the *MITE* in Figure 2.5 are both essentially flying wings with vertical tail surfaces for yaw stability.
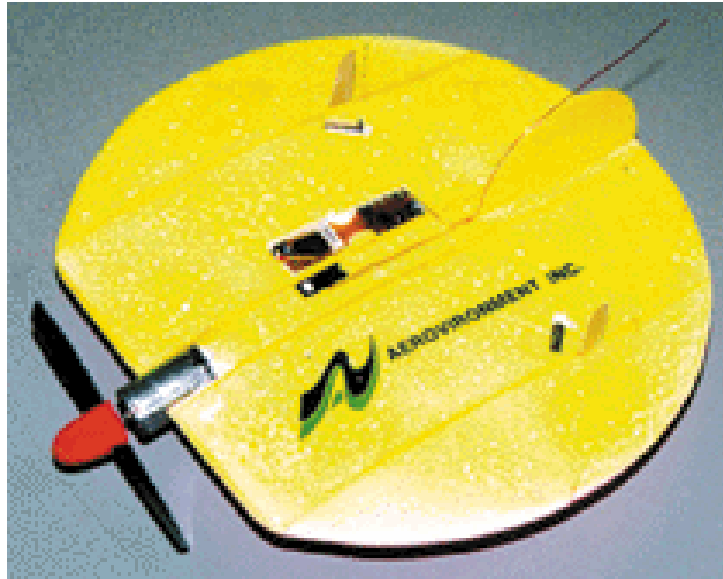
Figure 2.4. The *Black Widow* by Aerovironment.
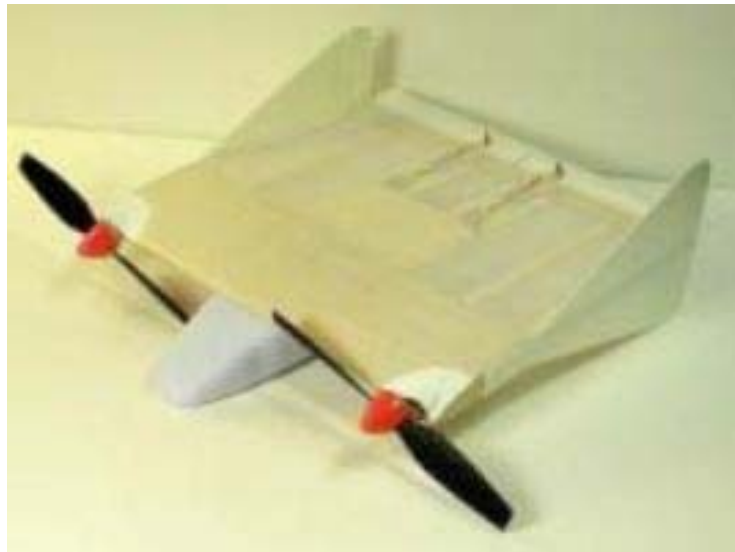
Figure 2.5. The Naval Research Laboratory's *MITE*.

Specific attention should be given to the *WASP* and the *HORNET* in Figure 2.6 and Figure 2.7 respectively, as neither include vertical tails for yaw control. The absence of these vertical tails implies that sideslip velocity was not an issue for the designers of these aircraft, and after consideration of this fact, the decision was made to neglect

vertical tails on the fixed wing MAV, flapping wing NAV with a tail, and tailless

flapping wing NAV in this study as well.

Figure 2.6. Aerovironment's *WASP*.
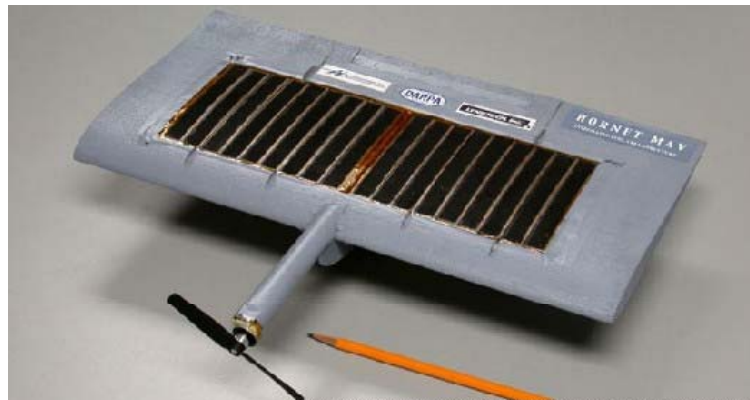
Figure 2.7. Aerovironment's *Hornet*.

It should be noted that although some aerodynamic tests have been performed

(specifically, the *MFI* has produced lift and thrust forces on a single wing), as of 1998

and 2003 the *Entomopter* and *MFI*, respectively, had not completed flights. Finally, the

MICOR [11] in Figure 2.8 and the *Mesicopter* [12] in Figure 2.9 are both rotor-based

MAVs while the *LuMAV* [13] and *iSTAR* [14] use ducted fans.
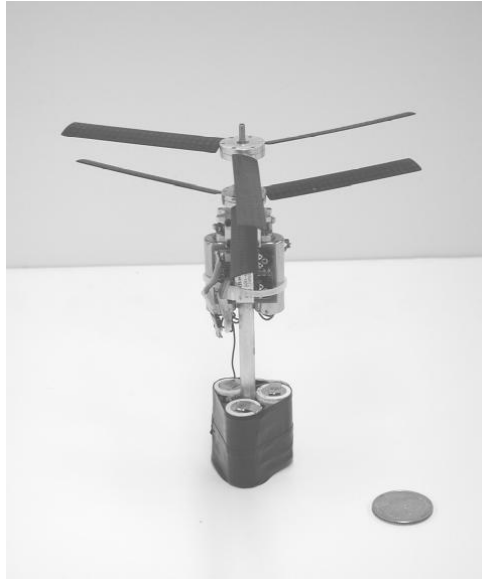
Figure 2.8. The *MICOR*.
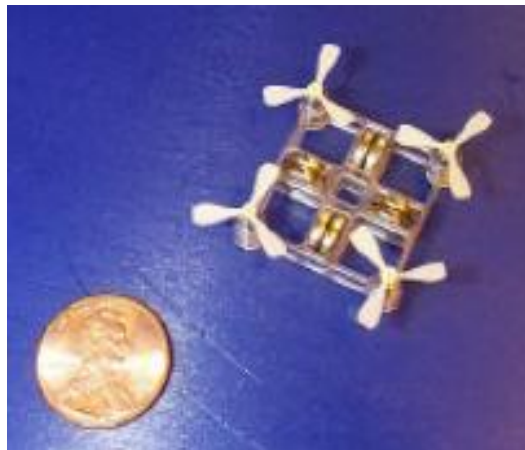
Figure 2.9. Battery Powered *Mesicopter*.

2.2. AIRCRAFT FUNCTIONAL MODEL

Functional modeling is a systematic way to relate system inputs, processes, and outputs through a generalized block diagram. For each function block of the diagram, a solution exists such that this solution corresponds to a physical device that can complete the desired function stated in the block. A generalized block diagram for a MAV is shown in Figure 2.10.
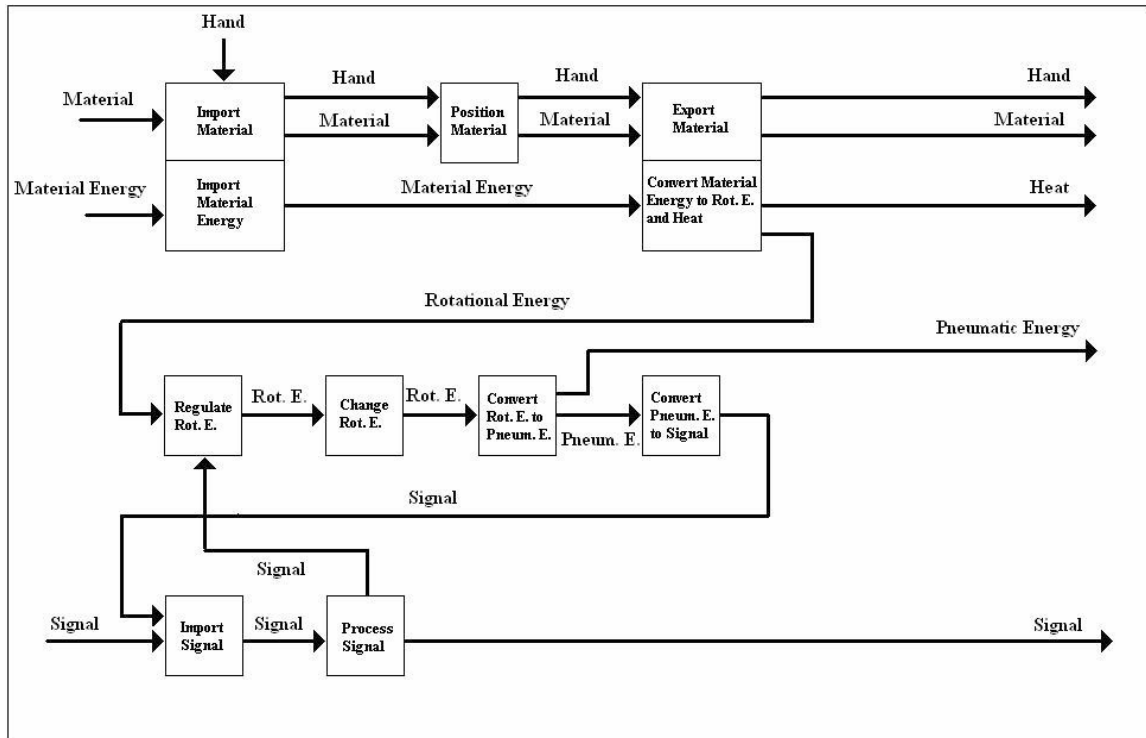
Figure 2.10. Functional Model for Generalized MAV.

Each action present in the blocks of the function model in Figure 2.10 was examined in depth with their respective solutions as found in the review literature in the following sections.

2.2.1. Import Material/Material Energy. Importing material simply refers to the gathering of the replaceable items; batteries, fuel, sunlight, etc. Due to the fact that the materials imported may be disposable batteries or fuel, the *Import Material* heading refers to replacing those items while *Import Material Energy* describes the inherit energy imparted to the system from those items. Disposable batteries are an excellent choice for an energy source in a MAV due to the relatively low expectations for flight time. The combustion configuration uses batteries in addition to fuel to power the electrical control systems.

The *Black Widow* uses rechargeable NiCd (Nickel-Cadmium) and NiMH (Nickel-Metal-Hydride) batteries for flight tests and a disposable Li (Lithium) battery for demonstration flights. The *Microbat* uses a rechargeable off-the-shelf Sanyo NiCd battery as well which produces 50 *mAhr* and weighs 3 *g*, while the *MITE* uses a Li-ion battery that has a capacity of 750 *mAhr*. In the *Mesicopter* program, multiple batteries were tested: the Energizer 2L76, Rayovac 361, and Rayovac 389. The Energizer arrangement in the system required two batteries connected in series to drive the four electric motors whereas 12 Rayovac 361 batteries or six Rayovac 389 batteries were required for the same four motors. The *MICOR* employs three 3 *V* LiMnO$_2$ batteries with a capacity of 430 *mAhr*. The *TH360* and *WASP* both incorporate self-designed batteries; the *TH360* uses a 600 *mAhr* NiMH battery and the *WASP* uses a Li-ion battery with an energy density of 143 *W/kg* and an average power output of 9 *W*. The *Palmtop* in Figure 2.11 and the *MicroSTAR* in Figure 2.12 are also expected to operate via batteries.
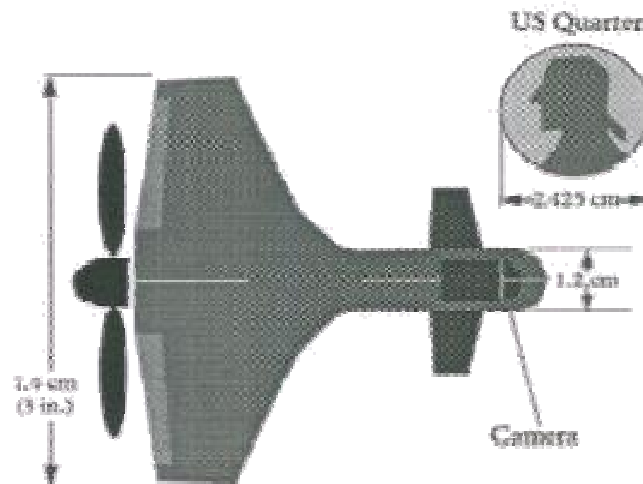
Figure 2.11. Conceptual Drawing of the *Palmtop*.

Figure 2.12. Conceptual Drawing of the Lockheed *MicroSTAR*.

The *Hornet* and *Indian* are the only reviewed MAVs that require no batteries.
The *Hornet* operates solely on a hydrogen-air mixture. Through power requirement
estimations, the *Indian* uses 490 *cm²* of solar panels to produce the predicted 4.9 *W*
needed while the *MFI* is expected to use both a battery and solar panels. Finally, the *ND*,
LuMAV, and *iSTAR* all use a battery along with hydro-carbon fuels for their internal
combustion engines (ICEs). Specifically, the *ND* in Figure 2.13 uses a 9 *V* NiCd battery
with a capacity of 50 *mAh*r. Only the *iSTAR* identifies its fuel, which is a mixture of
alcohol, nitro-methane, and oil.

Figure 2.13. Notre Dame's Most Recent MAV, Referred to as the *ND* in this Study.

2.2.2. Position Material. Given that the exact methods of the positioning techniques of the examined MAV are not specified, the solutions of this sub-function of the system are unclear. However, batteries are usually secured through a clamp of some sort and fuel is stored in a tank. The positioning of the solar panels on the *Indian* would be dictated by convenience of available area. While a seemingly tedious step in the functional modeling process, positioning is crucial to aerodynamic structural modeling, i.e. determining the center of mass, efficient use of available space, etc.

2.2.3. Export Material. Another vague area in the design process of the studied MAV, exporting materials indicates the method of removing used batteries and exhaust particles from the system. Rationale would point to disengaging any clamp or device used to hold batteries in position and piping of some kind to transport exhaust gases.

2.2.4. Convert Material Energy to Rotational Energy. After materials and their corresponding energies have been imported and positioned, the chemical, electrical, or solar energy must be converted to a mechanical energy before it can produce the required aerodynamic effects. As is probably apparent by now, the conversion of these energies comes from either an electric motor or an internal combustion engine. The *Black Widow*, *Microbat*, *MITE*, *TH360*, *MICOR*, *Mesicopter*, *MicroSTAR*, *Palmtop*, *Hornet*, *WASP*, and *Indian* all use or are expected to use electric motors; in fact, the *MICOR* has two electric motors and the *Mesicopter* has four. In particular, the *MICOR* utilizes a WES-Technik DC 9 *V* electric motor. The *ND* uses a Cox 0.01 *in^3* displacement internal combustion engine. While much of the information discovered on the *Entomopter* is vague, its primary contribution to the functional model is the Reciprocating Chemical Muscle (RCM), which is a solution of this energy conversion

function. The RCM uses a non-combustive chemical reaction to create mechanical motion, generate enough electricity to power onboard electrical components, and produce gas flows to improve aerodynamics. The *MFI* is expected to use a piezo-actuator to produce mechanical energy.

       2.2.5. Regulate Rotational Energy. Regulation of the rotational energy was specifically addressed in only three of the reviewed MAV, the *MFI*, *TH360*, and *LuMAV* in Figure 2.14. The *MFI* and *TH360* use electronic speed controllers incorporated into their control systems to regulate the speed of their motors and the *LuMAV* has a throttle servo. The remaining MAV undoubtedly regulate their mechanical energy, though it may be directly through their control systems like the *iSTAR* in Figure 2.15 which lists a voltage regulator.
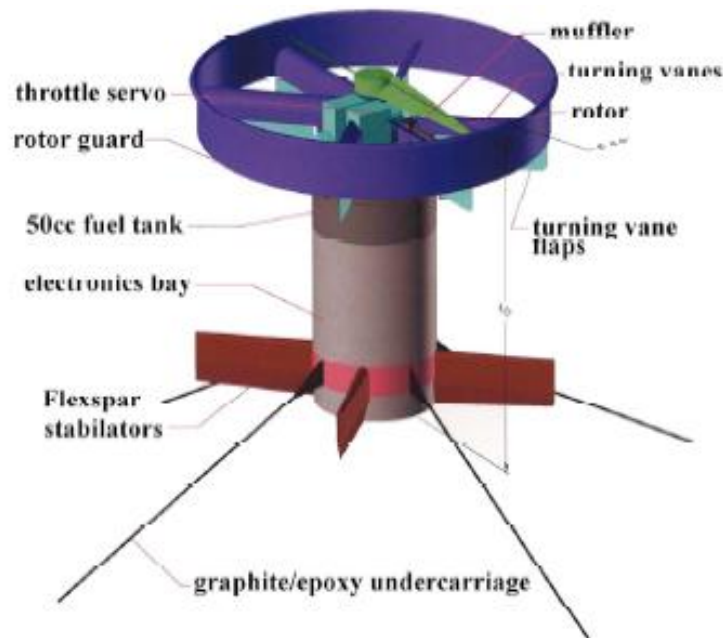
Figure 2.14. Conceptual Drawing of the *LuMAV*.

Figure 2.15. The *iSTAR*.

2.2.6. Change Rotational Energy. Changing the available rotational energy

implies the use of gears and/or linkage to amplify or diminish the output of the electric

motor or ICE. This output must be changed dramatically for the flapping wing models,

which leads to the use of a four-bar mechanism or linkage. These mechanisms can

directly prescribe the motion of the wings, as is expected in the *MFI*, or be used along

with gears, like the *Microbat*. While the *Entomopter* is a flapping wing model, its X-

wing system is directly coupled to the RCM. However, certain wing motion, like

feathering, is accomplished with the use of smart materials. The *Black Widow*, *TH360*,

MICOR, and *Indian* all use gearboxes to alter the outputs of their electric motor with

ratios of 4:1 for the *Black Widow*, 7:1 for the *TH360*, and 3.75:1 for each of the *MICOR*

motors. The *ND*, *MITE*, *iSTAR*, *Mesicopter*, *MicroSTAR*, and *Palmtop* specifically state

direct drives for their propellers.

2.2.7. Convert Rotational Energy to Pneumatic Energy. The conversion of energy is done through the use of propellers, wings, rotors, and actuators. When propellers are used, they produce thrust while the wings produce lift. In flapping models, the wings create both thrust and lift. The actuators are for use in rudders, elevators, and ailerons. The *LuMAV* system was indicated to be similar to its predecessor, the *Kolibri*, in that PZT-5A Flexspar stabilators are used to further control the pneumatic flows in the system. The *iSTAR* uses four COTS servos weighing 28 *g* apiece.

2.2.8. Convert Pneumatic Energy to Signal. The signal obtained here would be the position signal of the MAV. This signal is crucial to the control system for position correction. The *TH360* simply states that angular rate gyroscopes are used while the *Black Widow* lists a magnetometer, differential pressure sensors with a pitot tube, and a piezoelectric gyroscope. The *iSTAR* incorporates three Murata micro piezo-electric gyroscopes and the *LuMAV* (again based on the *Kolibri* system) uses 3 Tokin 16DIO piezoelectric gyroscopes. The remaining MAV undoubtedly have similar sensing devices, however, none are listed.

2.2.9. Import/Process Signal. Importing the signals to the MAV refers to a receiver picking up control signals from an external source (remote control). Processing that signal takes place in onboard computers of some sort, where the signal is put through a control algorithm. None of the reviewed MAV list a specific receiver or microprocessor.

2.2.10. Morphological Matrix. A morphological matrix is simply an array of the possible solutions for a given functional model. When designing, weights can be given to selected functions to emphasize more importance on this function. For instance, if a

certain function requires higher costs, larger mass, or greater occupied volume when implemented, it would be weighted heavier than other functions. For this study, the morphological matrix provided in Table 2.1 is simply a list of all of the known solutions produced from the reviewed MAV with no weights placed on the functions.

Table 2.1. Morphological Matrix for Studied MAV.

Functions	Solutions				
Import Material	Battery	Fuel	Hydrogen, Oxygen	Sunlight	Chemical
Position Material	Battery Clamp	Fuel Tank	-	-	-
Export Material	Release Clamp	Exhaust Pipes	-	-	-
Import Material Energy	Battery	Fuel	Water	Solar Panels	Chemical
Convert Material Energy to Rotation/Heat	Electric Motor(s)	ICE	Piezo Actuator	Reciprocating Chemical Muscle	-
Regulate Rotational Energy	Electric Speed Controller	Voltage Regulator	Throttle Servo	Stabilator	-
Change Rotational Energy	Gears	Linkage	4-Bar Mechanism	Direct	-
Convert Rotational Energy to Pneumatic Energy	Propeller and Wing	Actuators	Rotors	Rotor and Duct	-
Convert Pneumatic Energy to Signal	Gyroscopes	Piezo Gyroscopes	Pressure Sensors	Accelerometer	Magnetometer
Import Signal	Receiver	-	-	-	-
Process Signal	Microprocessor	-	-	-	-

3. DISCUSSION

3.1. RESEARCH METHOD

Recall from Section 1.2 that the first objective of this project was to develop a stable flapping wing aircraft using stability criterion methodologies from established fixed wing aircraft development. Then, using empirical data collected during testing on a wing developed by K. M. Isaac [15], dynamic models for both a flapping wing aircraft with a dummy tail and a tailless flapping wing aircraft were to be developed. Simulations were to be created to examine the stability and the flight capabilities of these aircraft. Several controller design approaches would also be examined for the first flapping wing aircraft. Finally, an estimation of the required power for the system would be made.

3.1.1. Stability Analysis. As stated earlier, this project began with the development of a statically stable fixed wing aircraft of MAV scale such that the established aircraft design processes could be introduced and examined for application to a flapping wing aircraft. After preliminary reading of aerospace texts, it became apparent that lift and drag properties can vary greatly between wings due to variations of wing properties like airfoil shape, aspect ratio, and sweep angle. Therefore, the wing used in testing by Isaac was used as the main wing for all three aircraft scenarios mentioned. This wing can be thought of as a flat-plate airfoil with a surface area that resembles half of an ellipse as seen in Figure 3.1. Throughout the rest of this paper, b_w (or b_t) is defined as a wing (or tail) span that includes both wings or tail fins. In Figure 3.1, c_w is the root chord length, which is mathematically defined later.
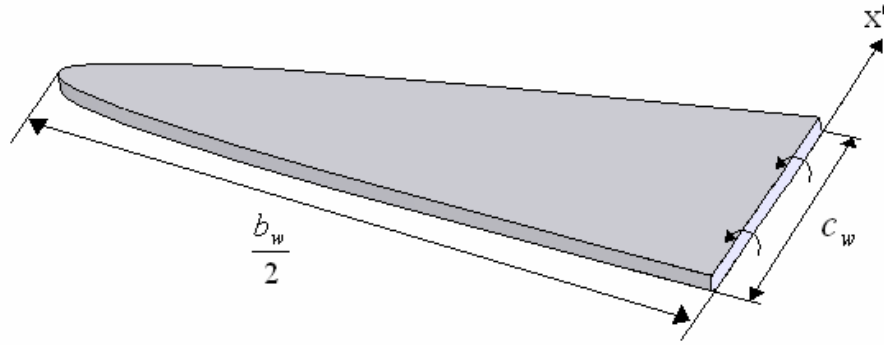
Figure 3.1. General Wing Used by Isaac; Rotation is About the *x'*-Axis.

Fixed wing design begins by calculating the horizontal tail geometric properties that correspond to the "rule of thumb" methods given in [16]. This method includes the use of empirical models developed by the aerospace industry over the years. Figure 3.2 shows the body-fixed frame coordinate system on the aircraft. Assuming that sideslip, fluid velocity along the *y*-axis, is negligible and that all maneuvers will be about the pitch axis, in the *xz*-plane, it is immediately apparent that a vertical tail is not necessary for this model. This assumption was reinforced by examining two balsa-wood and tissue paper models that were purchased online [19], and also by the *WASP* and *HORNET* mentioned earlier, as not one of these models implements a vertical tail for stability. The online models lend more authority to this decision than the *WASP* or *HORNET*, since both online models are actual flapping wing aircraft. In an actual environment where heavy sideslip velocities are present the aircraft being developed in this study, which is anticipated to have limited control capability due to size constraints, would probably not be able to overcome the yaw stability issues that arise anyway.

Following the method in [16], only a horizontal tail volume coefficient, c_{ht}, which is a constant developed for use in calculating tail area, and L_t, a general length that represents a moment arm, needed to be found for use in Equation 1.

$$S_t = \frac{c_{ht} S_w \bar{c}_w}{L_t} \qquad (1)$$

To determine c_{ht}, it was assumed that this aircraft resembled a sailplane such that $c_{ht} = 0.5$ from tables in [16]. As for L_t, this was approximated assuming, once again, that the aircraft was an unpowered sailplane with a maximum mass of 50 g. Using the approach in [16], this value was estimated as $L_t = (0.65)L_f$, where L_f is the length of the fuselage, which in the DARPA guidelines is bounded by 15 cm. To calculate these and the rest of the tail properties a few more quantities needed to be defined:

- The tail aspect ratio, A, was equal to the wing aspect ratio

- The tail taper ratio, $\lambda = 0.4$ (taken from an example in [16])

- The tail leading edge sweep, $\Lambda_{LE} = 12.6°$ (such that $\Lambda_{TE} = 0°$)

The aspect ratio is an important quantity that determines how aerodynamic surfaces' areas are distributed; in other words, if the wing is long and thin or short and fat. The wing used in modeling was a scaled down version of the wing Isaac used to collect his force data, and when scaling a wing either up or down, a constant aspect ratio is used to keep wing aerodynamic properties constant. Isaac's wing was a semi-ellipse, defined by a length-to-chord ratio, $(l_w/c_w) = 3$, where l_w is the wing length from the root

chord to the tip, and c_w is the root chord length. Again, the current project had a bound of 15 *cm* on total wing length, so $l_w = 0.075$ *m* in this case which, with the given length to chord ratio, corresponds to $c_w = 0.025$ *m*. The aspect ratio is defined in Equation 2, where S_w is the area of both wings and b_w is the total wing span.

$$A = \frac{\left(\frac{1}{2}b_w\right)^2}{\frac{1}{2}S_w} \qquad (2)$$

Note that the value of the aspect ratio using properties of one wing is half of the value when both wings are considered. For this study, the aspect ratio was calculated for one wing and that ratio was also used for the tail.

With a known chord length and wingspan, the area of a full ellipse (since both wings are used) was calculated by Equation 3 such that $S_w = 0.002945$ *m²*, and the aspect ration, A = 3.82.

$$S_w = \pi\left(\frac{b_w}{2}\right)\left(\frac{c_w}{2}\right) \qquad (3)$$

Therefore, with Equation 1 and $L_t = 0.0975$ *m*, $S_t = 0.000378$ *m²*. Finally, the following tail properties were calculated using equations found in or manipulated from [16] and the previously calculated or defined parameters.

$$b_t = 2\sqrt{\frac{1}{2}AS_t} = 0.054 \ m \qquad (4)$$

$$c_{rt} = \frac{2S_t}{b_t(1+\lambda)} = 0.01 \ m \qquad (5)$$

$$c_{tt} = \lambda c_{rt} = 0.004 \ m \qquad (6)$$

$$\bar{c}_t = \frac{2}{3}c_{rt}\frac{(1+\lambda+\lambda^2)}{1+\lambda} = 0.007 \ m \qquad (7)$$

In Equations 4-7, c_{rt} is the tail root chord length, c_{tt} is the tail tip chord length, and $\bar{c}_t$ is

the tail average chord length. These parameters can be seen on the tail provided in Figure

3.2.
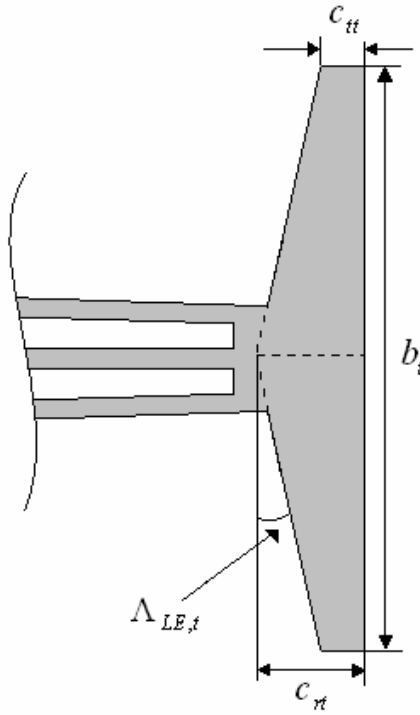
Figure 3.2. Aircraft Tail Parameters.

Once all of the tail geometric properties were calculated, the stability analysis

began. The first step in pitching stability analysis was to sum the moments created by

forces in the *xz*-plane about the center of mass for a general aircraft which in this case, assuming that the angle of attack is small, led to Equation 8.

$$M_{cg} = L_w\left(X_{cg} - X_{acw}\right) - L_t\left(X_{act} - X_{cg}\right) \qquad (8)$$

M_{cg} is the resultant moment about the center of mass, L_w and L_t are the lift forces generated by the wing and tail respectively, and X_{cg}, X_{acw}, and X_{act} are the positions of the aircraft center of mass, aerodynamic center of the wing, and aerodynamic center of the tail measured from the nose of the aircraft respectively, as seen in Figure 3.3. It is necessary to assume that the angle of attack is small in this stability analysis, because lift and drag are defined as acting perpendicular and parallel to the fluid velocity. Therefore, if the difference between the aerodynamic centers and the center of mass are to be used as moment arms, the aircraft moments are consequently created by forces along the *z*-axis, where these forces are actually vectors with components of both lift and drag.
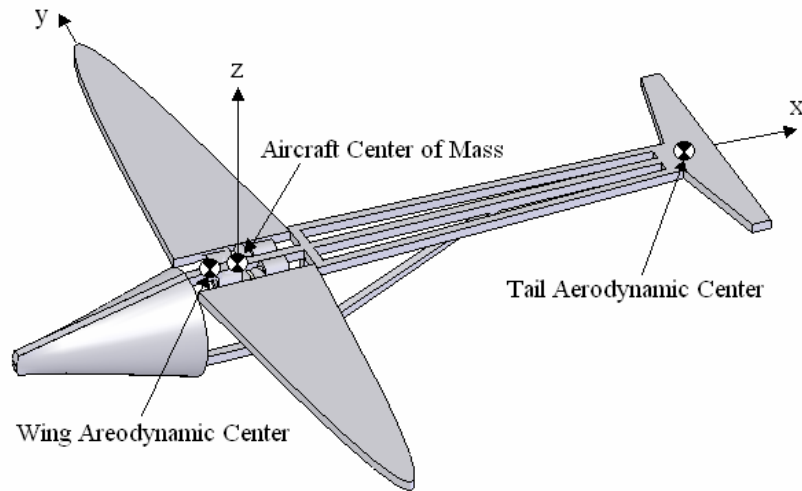
Figure 3.3. Body Frame Coordinate System on Concept Aircraft. Note that only the Lateral Positions of the Aerodynamic Centers are Given.

M_{cg}, L_w, and L_t are defined by Equations 9-11, where C_{mcg} is the moment coefficient about the center of mass, c_w is the wing root chord length, C_{Lw} is the wing coefficient of lift, C_{Lt} is the tail coefficient of lift, and q is the dynamic pressure, defined in Equation 12.

$$M_{cg} = qC_{m_{cg}}S_w c \qquad (9)$$

$$L_w = qC_{Lw}S_w \qquad (10)$$

$$L_t = q_t C_{Lt} S_t \qquad (11)$$

$$q = \frac{1}{2}\rho V_\infty^2 \qquad (12)$$

In Equation 12, ρ is the ambient fluid density and V_∞^2 is the ambient fluid velocity. Notice that the tail dynamic pressure term in Equation 11 is denoted with a subscript t, to indicate that the ambient velocity at the tail may be slightly different than at the wing due to upwash or downwash effects. When the equation is divided by $qS_w c$, the result is Equation 13.

$$C_{m_{cg}} = C_{Lw}\left(\overline{X}_{cg} - \overline{X}_{acw}\right) - C_{Lt}\eta_t\left(\overline{X}_{act} - \overline{X}_{cg}\right)\frac{S_t}{S_w} \qquad (13)$$

In Equation 13,

$$\overline{X} = \frac{X}{c_w} \qquad (14)$$

$$\eta_t = \frac{q_t}{q} \tag{15}$$

According to [16], the dynamic pressure ratio can be approximated as $\eta_t = 0.9$ for most cases. If the derivative is taken with respect to the aircraft angle of attack, α, the moment equation becomes

$$C_{m\alpha} = C_{Lw\alpha}\left(\overline{X}_{cg} - \overline{X}_{acw}\right) - \eta_t C_{Lt\alpha}\frac{\partial\alpha_t}{\partial\alpha}\left(\overline{X}_{act} - \overline{X}_{cg}\right)\frac{S_t}{S_w} \tag{16}$$

The partial derivative term here arises since the coefficient of lift of the tail cannot be directly differentiated with respect to the aircraft angle of attack α, due to upwash or downwash effects that arise from the deflection of the ambient fluid as it flows over the wing. In other words, the angle of attack at the tail is not the same as the angle of attack of the aircraft, and also changes in an unknown manner with respect to aircraft angle of attack variations.

After observing Equation 16, it was evident that "poles" and "zeros" that indicate the stability of linear mechanical systems were not necessarily useful (or easy to find) here. Instead, the aerospace approach to stability is to assess the value of $C_{m\alpha}$. Consider the case when $C_{m\alpha} = 0$; for every change in the angle of attack the aircraft is in static equilibrium as there are no net moments about the center of mass. If $C_{m\alpha} > 0$, there will be a net moment in the same direction so as to further increase the angle of attack, and therefore the system will become unstable. Therefore, it is desirable to have $C_{m\alpha} < 0$, so

for every change in the angle of attack, the aircraft will have a moment in the opposite

direction to try and drive the resultant aircraft moment back to zero.

To determine $C_{Lw\alpha}$ and $C_{Lt\alpha}$, equations found in [16] were used.

$$C_{Lx\alpha} = \frac{2\pi A}{2 + \sqrt{4 + \frac{A^2 \beta^2}{\eta^2}\left(1 + \frac{\tan^2(\Lambda_{max,t})}{\beta^2}\right)}}\left(\frac{S_{exp,x}}{S_x}\right)F_x \qquad (17)$$

$$\beta = 1 - M^2 \qquad (18)$$

$$\eta = \frac{C_{L\alpha}\beta}{2\pi} \approx 0.95 \qquad (19)$$

$$F_x = 1.07\left(1 + \frac{d_x}{b_x}\right)^2 \qquad (20)$$

M is the Mach number, which was approximated as $M = (10/340)$ since the

desired maximum forward speed was 10 m/s. [16] indicated that $\eta = 0.95$ was a good

estimate for most cases. In Equation 20, d_x is the diameter of the fuselage at the wing or

tail ($x = w$ for the wing and $x = t$ for the tail), which was estimated here as 3 cm at the

wing and 1 cm at the tail. This parameter must be considered since the fuselage inhibits

flow over the aerodynamic surface directly above it. $S_{exp,x}$ was subsequently calculated

by subtracting this area above the fuselage from the total surface area. Finally, Λ is the

wing or tail sweep, which was set to 0° for the wing. Since a taper ratio was used in tail

design, the trailing edge sweep for the tail was set to 0°, which resulted in a tail leading

edge sweep of $\Lambda_{LE,t} = 12.6°$.

It was desired that the final tail arrangement be a fairly common design, and for a novice aircraft designer the configuration seen in Figure 3.3 seemed a simple one. Inserting the previously calculated values of tail parameters and the known wing parameters into Equations 18-20, and then into 17, the coefficient of lift derivatives were found to be $C_{Lw\alpha}$ = 5.244 and $C_{Lt\alpha}$ = 5.136. Looking back at Equation 16, the partial derivative term and the $\overline{X}$ term still need to be quantified. The physical positions used to define the $\overline{X}$ terms can be seen in Figure 3.4. From empirical plots in [16], the partial derivative term can be conservatively estimated as

$$\frac{\partial \alpha_t}{\partial \alpha} \approx 0.67 \qquad (21)$$
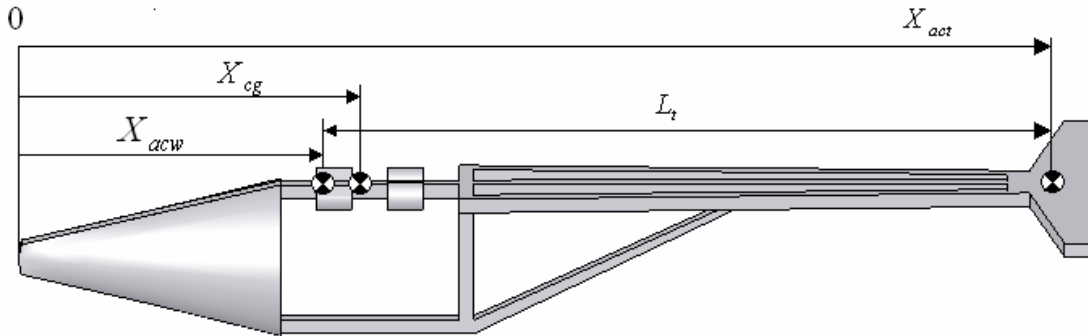
Figure 3.4. Important Parameter Positions on the Aircraft.

$\overline{X}_{act}$ was calculated by examining Figures 3.3 and 3.4 and knowing that forces on aerodynamic surfaces can be assumed to act at the mean aerodynamic chord, which is approximately one quarter chord length from the leading edge. Since the trailing edge of the tail was assumed to be at the maximum length from the nose, and seeing as the

trailing edge angle was $0°$, the aerodynamic center for the tail is located $\frac{3}{4}\bar{c}_t$ from the

trailing edge. Therefore,

$$X_{act} = \left(L_f - \tfrac{3}{4}\bar{c}_t\right) \tag{22}$$

Equation 22 leads to $X_{act} = 0.14475$ *m*, and combining this result with Equation

14, $\overline{X}_{act} = 5.79$. Remember also that all of these positions are measured from the nose of

the aircraft. Then, from the definition of L_t in [16] it was found that

$$X_{acw} = X_{act} - L_t \tag{23}$$

Equation 23 resulted in $X_{acw} = 0.04725$ *m* and $\overline{X}_{acw} = 1.89$. Determination of the

position of the center of mass was less cut and dry; in fact the center of mass's position at

this point determined the stability of the system. This analysis began by calculating the

neutral point, which was found by letting the moment coefficient derivative, $C_{m\alpha}$, in

Equation 16 equal zero and then solving for $\overline{X}_{cg}$ (which was denoted $\overline{X}_{np}$ during this

calculation). The neutral point is the most aft position for the center of mass on the

aircraft where the aircraft is not unstable. At this point, $C_{m\alpha} = 0$ and there are no net

moments about the aircraft. This is also known as trim condition.

$$\overline{X}_{np} = \frac{C_{Lw\alpha}\overline{X}_{acw} + \eta_t\left(\dfrac{S_t}{S_w}\right)C_{Lt}\alpha\dfrac{\partial\alpha_t}{\partial\alpha}\overline{X}_{act}}{C_{Lw\alpha} + \eta_t\left(\dfrac{S_t}{S_w}\right)C_{Lt\alpha}\dfrac{\partial\alpha_t}{\partial\alpha}} \qquad (24)$$

Substituting in known values, $X_{np} = 0.05412$ *m*. Since it was known that the

neutral point is the position of the center of mass where the system goes from stable to

unstable or vice versa, the difference between the actual location of the center of mass

and the neutral point can be thought of as a measure of the system stability, and is known

as the static margin.

$$\overline{X}_{cg} = \overline{X}_{np} - \overline{X}_{sm} \qquad (25)$$

Based on the examples in [16] a static margin, $\overline{X}_{sm}$, of 15% was selected, and thus

$\overline{X}_{cg}$ = 2.0148 and X_{cg} = 0.0504 *m* from Equation 14. Finally, substituting all of the

known and calculated values into Equation 16, the moment coefficient derivative was

calculated as $C_{m\alpha}$ = -0.846 which was acceptable since $C_{m\alpha}$ is negative.

This same process was repeated for an aircraft of NAV scale to develop the

geometrical properties of the two flapping wing aircraft, which can be seen in Table 3.1.

Note that no tail properties needed to be calculated for the tailless flapping wing aircraft,

and seeing as the wing properties remained the same for each flapping wing version, the

only difference between the two came about in the determination of the positions of the

aerodynamic centers and the center of mass. Due to the absence of the tail, the

aerodynamic center of the wing must be behind the center of mass on the tailless flapping

wing NAV. This is how a plane referred to as a "flying wing" maintains its stability.

Notice in Equation 16 that with the absence of the tail moment term, placing the wing

aerodynamic center behind the center of mass is the only way to force $C_{m\alpha}$ to be negative.

Table 3.1. Parameters for the Two NAV Scale Aircraft

Parameter	Symbol	NAV with Tail	NAV without Tail
Aircraft Length (m)	L_f	0.075	0.05
Wing Area, (m^2)	S_w	0.000736	0.000736
Tail Area, (m$_2$)	S_t	0.0000944	-
Mass, (kg)	m	0.01	0.01
Wing Root Chord (m)	c_w	0.0125	0.0125
Wingspan (m)	b_w	0.075	0.075
Tailspan (m)	b_t	0.027	-
Tail Root Chord (m)	c_{rt}	0.005	-
Tail Tip Chord (m)	c_{tt}	0.002	-
Tail Lift Coefficient Derivative	$C_{Lt\alpha}$	4.1985	-
Aircraft Positions (m)	X_{acw}	0.0234525	0.011875
	X_{cg}	0.02567	0.01
	X_{act}	0.0722025	-
Specific Principle Moments of Inertia (m^2)	I_{xx}	-	0.000136
	I_{yy}	0.00117	0.000136
	I_{zz}	-	0.000023

3.1.2. Dynamic Model. After the geometric and constant aerodynamic

parameters were calculated, the dynamic model of the fixed wing aircraft was developed

such that all of the system states' first order derivatives were mathematically related to

the states themselves. The states for this system were the aircraft inertial translational

positions, inertial angular positions, body translational velocities, and body angular

velocities. All of these states can be calculated for any time t with a simple numerical integrator.

First, the coordinate frames used in this model were defined. The inertial frame was fixed on the surface of the earth with the x-axis pointing north, the y-axis pointing east, and the z-axis pointing down. Next, a coordinate frame was put into the atmosphere (possibly, but not necessarily, at the aircraft center of mass) that translated with the aircraft center of mass, but stayed aligned with the inertial frame. Lastly, a body frame was attached to the aircraft center of mass that was allowed to yaw, pitch, and roll as well as translate with the aircraft. These frames were referred to as the inertial, atmospheric, and body frames respectively. The purpose of the atmospheric frame was to introduce "wind" velocities in the calculations, but no ambient wind velocities were considered for this project, so little else will be said about the atmospheric frame. Wind velocities can be added later on though, to account for specific flight conditions and produce a more realistic simulation. The aircraft body frame is the accompanying frame in Figure 3.3.

To relate the inertial velocities to the body frame velocities, Euler angles were implemented. A 3-2-1 Euler sequence was applied; the z-axis was rotated through an angle ψ, the resulting y-axis was rotated through an angle θ, and the following x-axis was rotated through an angle φ. Using these rotations, the transformation matrix that takes elements in the body frame into the inertial frame is

$$R_E^b = \begin{bmatrix} c_\psi c_\theta & c_\psi s_\theta s_\phi - s_\psi c_\phi & c_\psi s_\theta c_\phi + s_\psi s_\phi \\ s_\psi c_\theta & s_\psi s_\theta s_\phi + c_\psi c_\phi & s_\psi s_\theta c_\phi - c_\psi s_\phi \\ -s_\theta & c_\theta s_\phi & c_\theta c_\phi \end{bmatrix} \qquad (26)$$

In Equation 26, and many of the equations to follow, the form $s_x = sin(x)$ and $c_x = cos(x)$ is used to shorten the equation.

For a system with small deviations in ψ, θ, φ, the transformation matrix works well. However, if the angular displacements are large, the matrix can become singular. For the current aircraft, if the stability analysis was performed correctly, these angular displacements should not reach singular values (namely, θ should not approach $\dfrac{\pi}{2}$). In the case of hovering, θ may approach its singular value, depending on the aircraft orientation needed for this maneuver, and in that case the Euler rotations could be converted to quaternion rotations, which do not contain singularities.

The derivatives of the Euler angles are needed for system modeling, just as derivatives of the other states are needed in the system model. From the reading in [17],

$$
\begin{bmatrix} \dot{\psi} \\ \dot{\theta} \\ \dot{\phi} \end{bmatrix} = \begin{bmatrix} 0 & \dfrac{s_\phi}{c_\theta} & \dfrac{c_\phi}{c_\theta} \\ 0 & c_\phi & -s_\phi \\ 1 & \dfrac{s_\phi s_\theta}{c_\theta} & \dfrac{c_\phi s_\theta}{c_\theta} \end{bmatrix} \begin{bmatrix} \omega_x \\ \omega_y \\ \omega_z \end{bmatrix}
\tag{27}
$$

In Equation 27, ω_x is the body roll rate, ω_y is the body pitch rate, and ω_z is the body yaw rate. After examining Equation 27, the singularity of θ is much more apparent, since

$$
\frac{1}{\cos\left(\dfrac{\pi}{2}\right)} \to \infty
$$

Note that for both the fixed and flapping wing aircraft models, the six state equations

defined by Equation 27 and Equation 28, which relates the inertial and body velocities,

remain exactly the same.

$$\begin{bmatrix} \dot{x}_E \\ \dot{y}_E \\ \dot{z}_E \end{bmatrix} = R_E^b \bar{v}_b = R_E^b \begin{bmatrix} v_x \\ v_y \\ v_z \end{bmatrix} \qquad (28)$$

The remaining model was developed to provide the accelerations that arise from

the system forces and moments. Following the method in [18], Newton's second law can

be expressed as

$$m\left[\left(\frac{d\bar{v}_b}{dt}\right) + \bar{\omega}_b \times \bar{v}_b\right] = W^b + F_a^b \qquad (29)$$

$$I_b\left(\frac{d\bar{\omega}_b}{dt}\right) + \bar{\omega}_b \times I_b\bar{\omega}_b = M_a^b \qquad (30)$$

$\bar{v}_b$ is a column vector of the body velocity, and if the atmospheric frame was used, $\bar{v}_a$

would be the velocity of the ambient air in the atmospheric frame and $\bar{v}_{a/b}$ would be the

velocity of the aircraft relative to the atmosphere such that

$$\bar{v}_b = \left(R_E^b\right)^T \bar{v}_a + \bar{v}_{a/b} \qquad (31)$$

$\overline{\omega}_b$ in Equations 29 and 30 is a column vector of the body angular rates, W^b is the weight of the aircraft in the body frame with

$$W^b = \left(R_E^b\right)^T \begin{bmatrix} 0 \\ 0 \\ mg \end{bmatrix} = mg \begin{bmatrix} -s_\theta \\ c_\theta s_\phi \\ c_\theta c_\phi \end{bmatrix} \qquad (32)$$

F_a^b and M_a^b are the aerodynamic forces and moments to be defined later. Lastly, the I_b term is the inertia matrix of the aircraft in the body coordinate system, which in this study was comprised of only the principle moments of inertia. For those unfamiliar with the use of the body coordinate system, this inertia matrix is the primary reason for the body frame; if a frame was not affixed to an aircraft that translated, pitched, rolled, and yawed with the aircraft, the inertia matrix would have to be recalculated at every time step. For this aircraft only the inertia of the fuselage was considered, and the fuselage was assumed to be an ellipsoid with a diameter of 3 *cm* and a length of 15 *cm* such that

$$I_b = m \begin{bmatrix} I_{xx}' & 0 & 0 \\ 0 & I_{yy}' & 0 \\ 0 & 0 & I_{zz}' \end{bmatrix} = m \begin{bmatrix} 0.00117 & 0 & 0 \\ 0 & 0.00117 & 0 \\ 0 & 0 & 0.00045 \end{bmatrix} \qquad (33)$$

Note that the general moment of inertia term here was calculated by Equation 34 where *a* and *b* are some characteristic lengths of the aircraft.

$$I = \frac{1}{5}m\left(a^2 + b^2\right) \tag{34}$$

Hence, $I^{'}$ represents a specific moment of inertia, or a moment of inertia with the mass term factored out. The inverse of the inertia matrix is

$$I_b^{-1} = \frac{1}{m}\begin{bmatrix} \dfrac{1}{I_{xx}^{'}} & 0 & 0 \\ 0 & \dfrac{1}{I_{yy}^{'}} & 0 \\ 0 & 0 & \dfrac{1}{I_{zz}^{'}} \end{bmatrix} \tag{35}$$

After substituting Equations 32-35 into 29 and 30, expanding the cross-product terms, and solving for $\left(\dfrac{d\bar{v}_b}{dt}\right)$ and $\left(\dfrac{d\bar{\omega}_b}{dt}\right)$

$$\begin{bmatrix} \dot{v}_x \\ \dot{v}_y \\ \dot{v}_z \end{bmatrix} = g\begin{bmatrix} -s_\theta \\ c_\theta s_\phi \\ c_\theta c_\phi \end{bmatrix} + \frac{1}{m}\begin{bmatrix} F_x \\ F_y \\ F_z \end{bmatrix} + \begin{bmatrix} \omega_z v_y - \omega_y v_z \\ \omega_x v_z - \omega_z v_x \\ \omega_y v_x - \omega_x v_y \end{bmatrix} \tag{36}$$

$$\begin{bmatrix} \dot{\omega}_x \\ \dot{\omega}_y \\ \dot{\omega}_z \end{bmatrix} = \begin{bmatrix} \dfrac{1}{I_{xx}^{'}}\left\{\dfrac{1}{m}M_x + \omega_z\omega_y\left(I_{yy}^{'} - I_{zz}^{'}\right)\right\} \\ \dfrac{1}{I_{yy}^{'}}\left\{\dfrac{1}{m}M_y + \omega_x\omega_z\left(I_{zz}^{'} - I_{xx}^{'}\right)\right\} \\ \dfrac{1}{I_{zz}^{'}}\left\{\dfrac{1}{m}M_z + \omega_x\omega_y\left(I_{xx}^{'} - I_{yy}^{'}\right)\right\} \end{bmatrix} \tag{37}$$

Equations 27, 28, 36, and 37 contain the 12 first-order, nonlinear equations necessary to represent the aircraft dynamics for all three cases. The difference between the three cases lies in the determination of F_a^b and M_a^b.

3.1.3. Aerodynamic Forces and Moments. For the fixed wing aircraft, the calculation of F_a^b and M_a^b was fairly straightforward. Beginning with F_x, this aerodynamic force can be thought of as the drag on the aircraft. As of yet, no drag coefficients have been determined for the plane in this writing. According to [16] there are numerous types of drag that can be considered, but for this novice design pass only the parasite drag, which is dependent on some constant value, C_{D0}, and drag due to lift, KC_L^2, was considered. With these two types of drag, C_D is defined in [16] by Equation 38, where Equations 39 and 40 are used to simplify the expression to Equation 41.

$$C_D = C_{D0} + KC_L^2 \qquad (38)$$

$$K = \frac{1}{C_{L\alpha}} \qquad (39)$$

$$C_L = C_{L\alpha}\alpha \qquad (40)$$

$$C_D = C_{D0} + C_{L\alpha}\alpha^2 \qquad (41)$$

Letting C_{D0} = 0.05, Equation 41 becomes an equation for drag in terms of known parameters. α is strictly defined as the aircraft angle of attack, which was quantified as the angle between the aircraft's horizontal axis (x-axis) and the ambient fluid. Therefore,

$$\alpha = \tan^{-1}\left(\frac{v_z}{v_x}\right) \tag{42}$$

Notice from Figure 3.4 that v_x should always be negative in this project. Hence, a negative v_z will produce a positive angle of attack. This intuitively makes sense. When looking at the velocity terms, it may seem that since this angle is based only on the aircraft velocity, there may be need for another term to consider the aircraft orientation. But since the body frame rotates with the aircraft, Equation 42 incorporates the plane's orientation and is indeed the angle of attack. In fact, in [16], the only definition of α equates the derivative of the angle of attack with respect to time to the pitch rate, ω_y. The angle of attack for a flapping wing was significantly more difficult to quantify with this method since all of the angular velocities of the wing were not presently known, which is why the definition from [16] was not used. In fact, for a more precise model, all of the body angular rates should be included in calculation of the angle of attack and in system damping. Other than the pitch rate though, the body angular rates were assumed negligible so as not to contribute to an effective angle of attack, which leads to damping. In fact, system damping was neglected as it would increase complexity; any results without damping could be considered at the very least a worse case scenario anyway.

That being the case, Equation 42 is an accurate representation of the aircraft angle of attack, although the angle of attack of the wing and tail varied slightly from Equation 42 due to the incidence angles of these surfaces. Incidence angles arise at the wing, for instance, when the wing is built at some angle with respect to the x-axis of the aircraft. These incidence angles were labeled α_w and α_t for the wing and tail, respectively.

Although incidence angles may seem unimportant, they are an integral part of aircraft flight, especially steady level flight.

During steady level flight, the aircraft flies at a constant altitude and velocity. If no incidence angles are present, the tail moment would always be greater than the moment created by the wing. Therefore the aircraft would always try to drive α to zero (since $C_{M\alpha} < 0$ from the stability analysis). Once $\alpha = 0$, there would be no lift without an incidence angle and therefore the aircraft would rotate, dive, and repeat the process. Hence, the incidence angles allow the wing moment to equal the tail moment at a non-zero α, which means that lift will still be present for level flight.

Recall from Section 3.1.1 that the aerodynamic vertical and horizontal forces acting on the wing and tail are not simply lift and drag, since lift is perpendicular to the ambient airflow and drag is parallel as shown in Figure 3.5. Note however, that Figure 3.5 simply shows lift and drag directions with respect to airflow on the aircraft body; when the wing and tail are considered, the incidence angles must be added to the angle of attack to calculate the vertical and horizontal forces.
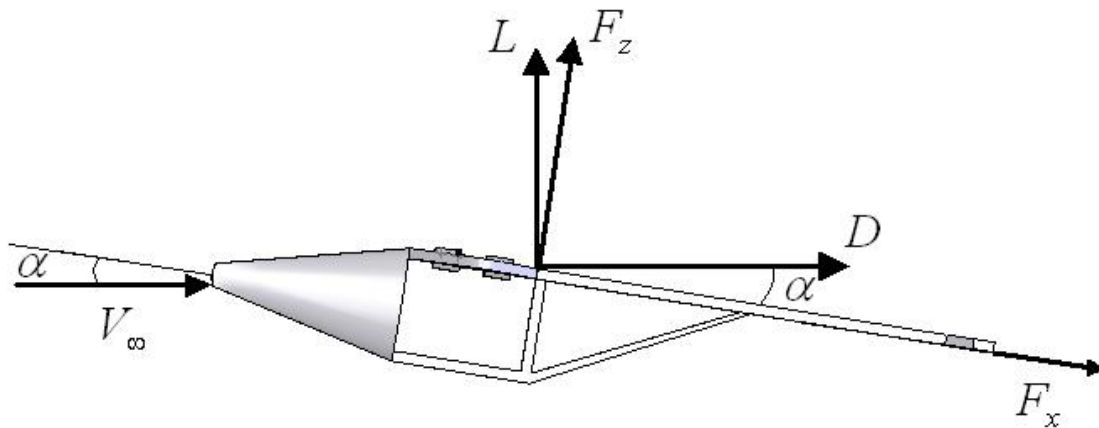
Figure 3.5. Relationship of Aerodynamic Forces.

The terms for the lift and drag on the tail and wing are

$$L_w = \frac{1}{2}\rho C_{Lw\alpha}(\alpha_w + \alpha)S_w V_\infty^2 \qquad (43)$$

$$L_t = \frac{1}{2}\rho C_{Lt\alpha}(\alpha_t + \alpha)S_t V_\infty^2 \qquad (44)$$

$$D_w = \frac{1}{2}\rho\left\{C_{D0} + C_{Lw\alpha}(\alpha_w + \alpha)^2\right\}S_w V_\infty^2 \qquad (45)$$

$$D_t = \frac{1}{2}\rho\left\{C_{D0} + C_{Lt\alpha}(\alpha_t + \alpha)^2\right\}S_t V_\infty^2 \qquad (46)$$

V_∞^2 is the square of the magnitude of the aircraft velocity, $V_\infty^2 = v_x^2 + v_z^2$. Since it was

stated earlier that the atmospheric velocities were assumed to be zero, V_∞ is the fluid

velocity as well. Although the sideslip velocity, v_y, is a state that may possibly have a

non-zero value due to inertial and gravitational forces, it was assumed earlier that the

sideslip velocity would be negligible such that $F_y = 0$. Therefore, using Figure 3.5 as a

basis and assuming that the aircraft thrust, T, acts along the x-axis, the vertical and

horizontal forces for the fixed wing aircraft can be expressed as

$$F_x = D_w \cos(\alpha_w + \alpha) + D_t \cos(\alpha_t + \alpha) - L_w \sin(\alpha_w + \alpha) - L_t \sin(\alpha_t + \alpha) - T \quad (47)$$

$$F_z = L_w \cos(\alpha_w + \alpha) + L_t \cos(\alpha_t + \alpha) + D_w \sin(\alpha_w + \alpha) + D_t \sin(\alpha_t + \alpha) \quad (48)$$

As for the aerodynamic moments acting on the aircraft, the yaw moment is based

on the sideslip, so $M_z = 0$. The roll moment is based on unbalanced lift forces, and since

there were no control surfaces in this model to incorporate unbalanced forces, $M_x = 0$.

That left the pitching moment, so considering the vertical forces acting on the wing and

tail, and the positions of the wing and tail aerodynamic centers and the center of mass,

$$M_y = \{L_w \cos(\alpha_w + \alpha) + D_w \sin(\alpha_w + \alpha)\}X_w - \{L_t \cos(\alpha_t + \alpha) + D_t \sin(\alpha_t + \alpha)\}X_t$$

(49)

$$X_w = X_{cg} - X_{acw}$$ *(50)*

$$X_t = X_{act} - X_{cg}$$ *(51)*

All of the forces and moments defined above were inserted into the differential

Equations 36 and 37 for the final fixed wing dynamic system. During early simulation of

this system, the parameters α_w, α_t, T, and the state initial conditions were varied to see

if the system behaved appropriately. However, this system is highly nonlinear, and

without an extensive background in aerospace, an intuitive feel for the appropriate

response was not possible. Therefore, a base checkpoint was considered; steady-level

flight. If a constant T, α_w, α_t, and initial conditions could be calculated which produced

steady-level flight, variation of the aforesaid parameters from these values should

produce easily anticipated results.

For steady-level flight, there should be no rotations, accelerations, or translation

in the z-direction. This leads to

$$\dot{x}, \dot{y}, \dot{z}, \dot{\psi}, \dot{\theta}, \dot{\phi}, \dot{v}_x, \dot{v}_y, \dot{v}_z, \dot{\omega}_x, \dot{\omega}_y, \dot{\omega}_z, \psi, \theta, \phi, v_y, v_z, \omega_x, \omega_y, \omega_z, \alpha = 0 \qquad \forall\, t \geq 0$$

$\alpha = 0$ since $v_z = 0$, and based on the earlier discussion of incidence angles, this makes sense. After all of the above values were substituted into Equations 27, 28, 36, and 37 the remaining equations were

$$\dot{\omega}_y = \frac{1}{I_{yy}'m} M_y = 0 \tag{52}$$

$$\dot{v}_z = \frac{1}{m} F_z - g = 0 \tag{53}$$

$$\dot{v}_x = \frac{1}{m} F_x = 0 \tag{54}$$

Letting $b_1 = \frac{1}{2}\rho C_{Lw\alpha} S_w$, $b_2 = \frac{1}{2}\rho C_{Lt\alpha} S_t$, $b_3 = \frac{1}{2}\rho C_{D0} S_w$, $b_4 = \frac{1}{2}\rho C_{D0} S_t$, and

again using the form $c_x = cos(x)$ and $s_x = sin(x)$, Equations 52-54 simplify to

$$X_w \left\{ b_1 \alpha_w c_{\alpha w} + \left(b_3 s_{\alpha w} + b_1 \alpha_w^2 \right) s_{\alpha w} \right\} - X_t \left\{ b_2 \alpha_t c_{\alpha t} + \left(b_4 + b_2 \alpha_t^2 \right) s_{\alpha t} \right\} = 0 \tag{55}$$

$$V_\infty^2 = v_x^2 = \frac{mg}{b_1 \alpha_w c_{\alpha w} + \left(b_3 + b_1 \alpha_w^2 \right) s_{\alpha w} + b_2 \alpha_t c_{\alpha t} + \left(b_4 + b_2 \alpha_t^2 \right) s_{\alpha t}} \tag{56}$$

$$T = v_x^2 \left\{ \left(b_3 + b_1 \alpha_w^2 \right) c_{\alpha w} + \left(b_2 + b_4 \alpha_t^2 \right) c_{\alpha t} - b_1 \alpha_w s_{\alpha w} - b_2 \alpha_t s_{\alpha t} \right\} \tag{57}$$

Selecting a likely value for α_w, Equation 55 was solved with the built in Matlab command *fsolve*. Once α_t was found, α_w and α_t were inserted in Equation 56 to find the initial condition of v_x. Finally, with α_w, α_t, and v_x, Equation 57 could be solved for the necessary thrust, T, required for steady-level flight.

3.1.4. Time Dependent Empirical Coefficients. Note that the form of the

dynamic model in Equations 27, 28, 36, and 37 remained the same for the flapping wing

aircraft, although the terms V_{eq}^2, α_{eq}, C_L, C_D, C_f, β, and s_n are added to calculate the wing

forces now. The terms C_L, C_D, and C_f were used to replace the constant coefficient

derivatives used for the fixed wing aircraft such that $C_{Lw\alpha} = f_1(t)$ and $C_{Dw\alpha} = f_2(t)$.

If at this point there is uncertainty as to why there is a need of these derivative

terms (since most mechanical engineers are more familiar with coefficients of lift and

drag) simply think of holding a hand out of a vehicle window while riding in a car. If the

hand is held perfectly level, there is little or no lift upward force. If the hand is held at a

small upward angle, there is a force felt up. This force increases as the angle increases.

It is evident that the coefficients of lift and drag are a function of the angle of attack.

These coefficients are functions of other parameters as well, such as the aspect ratio,

taper ratio, and wing sweep, but the effects from these latter factors are usually

considered negligible.

As there were no methods in [16] for developing these coefficients for a flapping

wing, it was evident from the data in [15] that the normal force on the test wing, and

therefore the lift and drag coefficients, varied throughout the stroke. In fact, upon

observation, it was immediately obvious that the data resembles a time-dependent

sinusoid. A sample of Isaac's actual data can be found in Figure 3.6, and a general plot

of the force data used to determine a time dependent function is given in Figure 3.7.

The green vertical bars in both figures represent a pitching phase, or reversing of

direction of the wing. With this knowledge and an examination of Figure 3.6, it was

apparent that the frequency for the force sinusoid was twice the flapping frequency. This

is because the force normal to the wing starts at zero at what can be assumed is the

bottom of the stroke angle (at the first green bar). As the stroke angle reaches its

maximum value (at the second green bar), the force has returned to zero. When the wing

returns the its starting position (at the third green bar), the force has once again returned

to zero.
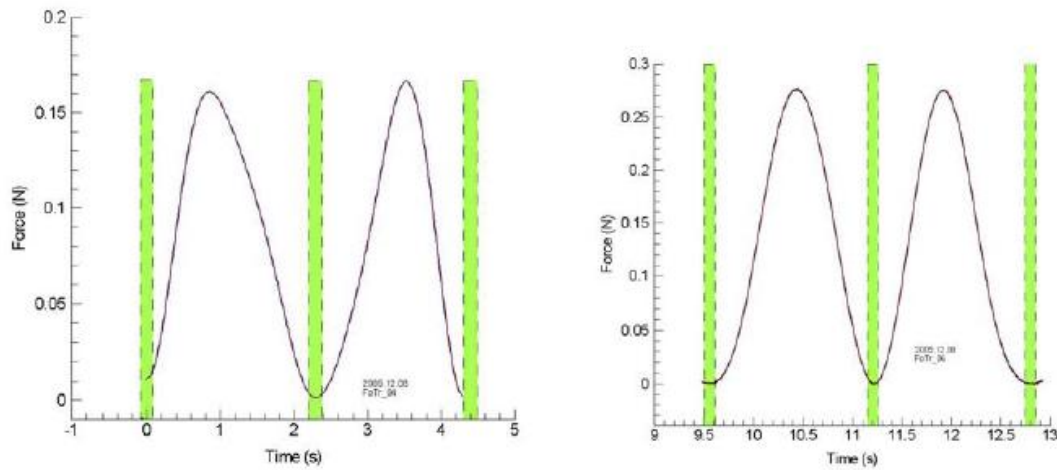
Figure 3.6. Isaac's Data; the Left Plot is the Force Normal to a Wing Flapping at 0.22 Hz
and the Right Plot is at 0.29 Hz. Both Wings have an Angle of Attack of 30°.
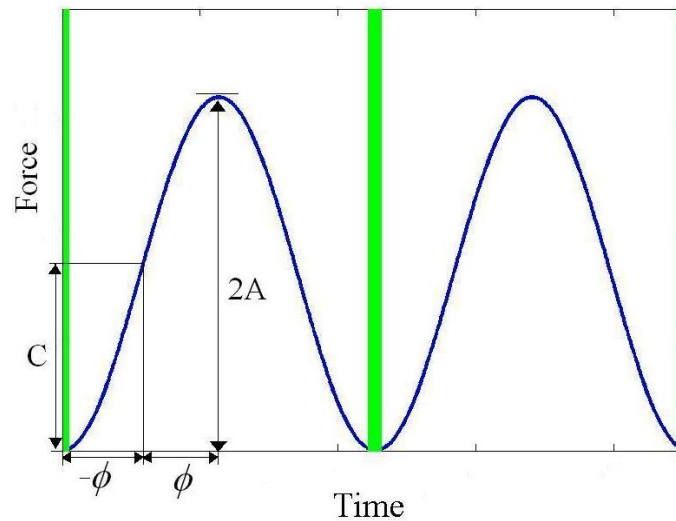
Figure 3.7. General Sinusoid used to Approximate Time-Dependent Force Functions.

Therefore, each time the wing completes one cycle, the force function has completed two cycles. That being stated, the normal force function for a set of data was approximated as

$$F_n = C + A\sin(\omega t + \phi) \qquad (58)$$

Note that the desired starting point for flapping is at the mid-stroke (wings aligned with the aircraft horizontal axis). This point is halfway between the first and second green bars in Figure 3.7, which is the peak of the sinusoid, so $\phi = \dfrac{\pi}{2}$. Recall the trigonometric identity $\cos(x) = \sin\left(x + \dfrac{\pi}{2}\right)$. Also, since the sinusoid minimum is $F_n = 0$, $C = A$ for this case, and $\omega = 2\pi f_d$ where f_d is the frequency of the data. As stated above, this frequency is twice the flapping frequency f, so the final force function was defined as

$$F_n = A(1 + \cos(4\pi ft)) \qquad (59)$$

After initially calculating these functions, the leading coefficient of the function was multiplied by either sine or cosine of the angle of attack that the data was collected at to arrive at the lift and drag functions

$$L_{f,\alpha} = F_n \sin\alpha \qquad (60)$$

$$D_{f,\alpha} = F_n \cos\alpha \qquad (61)$$

The coefficients of lift and drag were then calculated for each set of data by dividing Equations 60 and 61 by the dynamic pressure and area of the wing. A derivative function with respect to the angle of attack was calculated by subtracting the coefficient of lift at one angle of attack from the coefficient of lift at the other and then dividing by the difference in the angles.

$$C_{L\alpha} = \frac{C_L(\alpha_1) - C_L(\alpha_2)}{\alpha_1 - \alpha_2} \qquad (62)$$

The coefficient of drag derivative is calculated in a similar manner. This will all be shown shortly; the reason for this explanation is that once these steps were completed, an arbitrary time was chosen and each function was evaluated at this time. The result was multiplied by its corresponding angle of attack and dynamic pressure, and then divided by either $\cos \alpha$ or $\sin \alpha$. The resulting value should have corresponded to the actual data at that time. While the end result from the functions derived from the data at 0.22 *Hz* correlated quite well with the actual data, the same could not be said for the functions for 0.29 *Hz*. Therefore, the functions used to develop the coefficient derivatives at this time were based solely on the 0.22 *Hz* data.

The coefficient for Equation 59 for both angles of attack at 0.22 *Hz* was estimated as $A_{30°} = 0.08$ and $A_{45°} = 0.11$. Recall in normal applications, $L = F_n \cos \alpha$ and $D = F_n \sin \alpha$, where the lift will be perpendicular to the fluid flow and the drag will be parallel to the fluid flow. In this project's application however, the wing is assumed to be flapping in a stroke plane that is perpendicular to the forward velocity of the aircraft and

therefore the lift from these equations will actually be the system drag while the drag from these equations will be the system lift, hence the reversal of sine and cosine in Equations 60 and 61.

Multiplying these coefficients by $\sin\alpha$ for lift and $\cos\alpha$ for drag creates four equations: two lift equations corresponding to the two angles of attack, and two drag equations corresponding to the two angles of attack. Notice that dividing Equation 59 by some constant only changes the leading coefficient, so the four new coefficients were:

- $A_{L30°} = 0.04$

- $A_{L45°} = 0.077782$

- $A_{D30°} = 0.069282$

- $A_{D45°} = 0.077782$

To compute the time dependent coefficient derivatives, the coefficient for the lift function at 30° was subtracted from the coefficient of the lift function at 45° and the resulting difference was divided by the difference in angles. The drag coefficient derivative was computed the same way, and the final coefficient derivatives were Equations 63 and 64, where $C_L = 3.41445$ and $C_D = 0.768145$.

$$C_{Lw\alpha} = 3.41445\left(1 + \cos(4\pi ft)\right) = C_L C_f \tag{63}$$

$$C_{Dw\alpha} = 0.768145\left(1 + \cos(4\pi ft)\right) = C_D C_f \tag{64}$$

$$C_f = 1 + \cos(4\pi ft) \tag{65}$$

The fluid velocity at the wing also changes when a flapping wing is used. The velocity still has components of both v_x and v_z from the body velocities, but also from the flapping velocity of the wing. Therefore, the equivalent velocity at the wing is defined in Equation 66, where v_f^2 is the square of the flapping velocity.

$$V_{eq}^2 = v_f^2 + v_x^2 + v_z^2 \tag{66}$$

The flapping velocity is defined in [1] be Equation 67, where ψ is the stroke angle in radians, l_c is the length of the wing from the wing pivot to the mean chord, and f is the flapping frequency.

$$v_f = 2l_c \psi f \tag{67}$$

The angle of attack of the flapping wing cannot merely be thought of as $\alpha = \tan^{-1}\left(\dfrac{v_z}{v_x}\right)$ anymore, because the velocity at the wing has components from v_x, v_z, and v_f. Knowing the components of the equivalent velocity, the equivalent angle of attack in Figure 3.8 was defined as

$$\alpha_{eq} = \alpha_0 s_n - \tan^{-1}\left(\frac{v_f s_n + v_z}{-v_x}\right) = \alpha_0 s_n - \beta \tag{68}$$
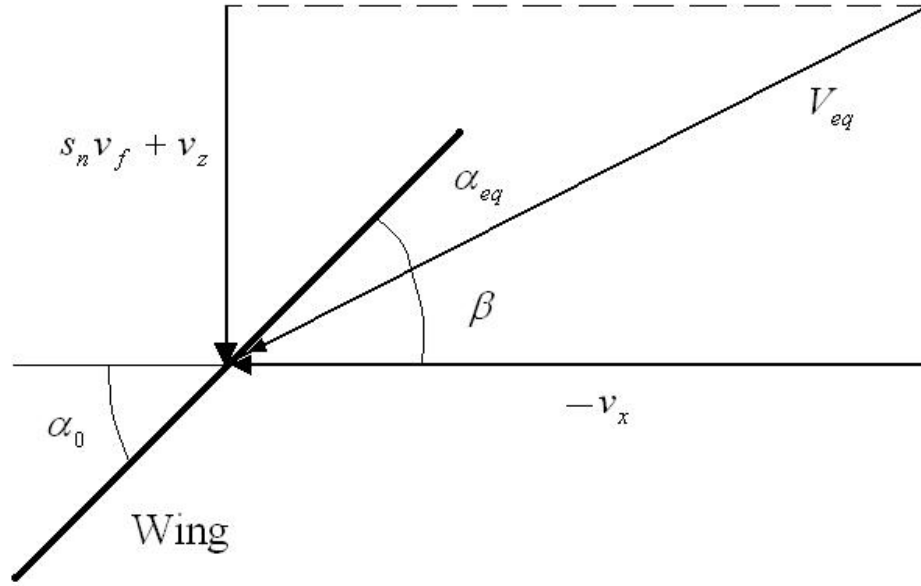
Figure 3.8. Schematic used to Calculate α_{eq} in Terms of Fluid Velocities.

α_0 is an input to the system which corresponds to the angle of the wing measured from the negative x-axis. For the flapping wing aircraft with a tail this value was the same for both wings, where the tailless flapping wing aircraft separated α_0 into α_L and α_R to calculate each wings forces independently.

s_n is a signum function that determines the sign of the flapping velocity throughout the stroke. In other words, if the wing is in the upstroke, $s_n = 1$ and if it is in the downstroke $s_n = -1$. Mathematically,

$$s_n = \text{sgn}\left(\sin\left(2\pi f t\right)\right) \tag{69}$$

The negative sign has to be applied to the v_x velocity since a positive v_x is along a negative x-axis in a normal Cartesian coordinate system.

In Figure 3.8, the velocities used to calculate α_{eq} were the fluid velocities, which are the negative of the body velocities. The term $s_n v_f + v_z$ was used to emphasize a net positive body velocity along the z-axis. If both velocity components were reversed in Figure 3.8, both would correspond to velocities in the positive direction of the axes of a Cartesian coordinate system. These reversed velocities were then related to actual body velocities to apply the correct signs to Figure 3.8. Note that as long as both velocities are reversed, any resulting term calculated with these velocities will remain correct. In the case of Figure 3.8, the velocity along the z-axis would be a positive velocity in body coordinates, and the velocity along the x-axis would be a negative v_x in body coordinates. Along with the negative sign applied to v_x, this would result in a positive β according to Equation 68.

When compared with the definition of the angle of attack, this would seem wrong. Examining Figure 3.8, β should be a negative angle regardless of α_0, since it is acting downward on the x-axis. But notice the conflicting way that α_0 and α are measured; α is positive below the x-axis, and α_0 is measured positive above. Using this method, if β was measured in the same way as α, then β would have to be added to α_0 to obtain the correct equivalent angle of attack. This definition of α_{eq} would confuse most readers, and therefore it was easier to define α_{eq} by subtracting a positive value rather than adding a negative. In fact, the latter case here is still what was performed, because

$$\tan^{-1}(x) = -\tan^{-1}(-x).$$

The last step in developing the flapping wing aircraft parameters was to determine the vertical and horizontal forces acting on the aircraft in the body frame as components of the aircraft lift and drag. This was done in much the same way that the vertical and

horizontal forces were determined for the fixed wing aircraft, and in fact the vertical and horizontal forces acting on the tail remained exactly the same. A schematic of the forces acting on the flapping wing can be seen in Figure 3.9.

Following Figure 3.9, the vertical and horizontal forces for the flapping wing were found to be

$$F_{wx} = D_w \cos \beta + L_w \sin \beta \qquad (70)$$

$$F_{wz} = L_w \cos \beta - D_w \sin \beta \qquad (71)$$
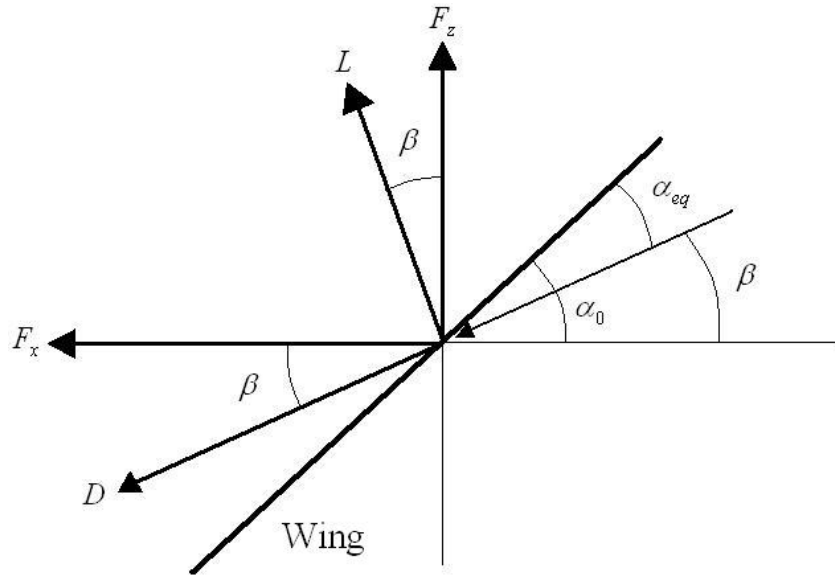
Figure 3.9. Schematic to Calculate Vertical and Horizontal Forces on Flapping Wing.

Combining these with the vertical and horizontal forces at the tail as defined in the previous section, the vertical and horizontal forces and the moment acting on the flapping wing aircraft are

$$F_x = D_w \cos\beta + L_w \sin\beta + D_t \cos(\alpha_t + \alpha) - L_t \sin(\alpha_t + \alpha) \qquad (72)$$

$$F_z = L_w \cos\beta - D_w \sin\beta + D_t \sin(\alpha_t + \alpha) + L_t \cos(\alpha_t + \alpha) \qquad (73)$$

$$M_y = (L_w \cos\beta - D_w \sin\beta)X_w - \{L_t \cos(\alpha_t + \alpha) + D_t \sin(\alpha_t + \alpha)\}X_t \qquad (74)$$

Notice in Equations 70 and 71 that the signs for the flapping wing alternate from the signs for the tail (or fixed wing). This is because a positive α for the fixed surfaces is below the x-axis, while a positive β is above the x-axis due to the way β was defined. While the lift and drag terms for the tail in Equations 44 and 46 were used again in Equations 72 and 73, the lift and drag terms for the wing became

$$D_w = \frac{1}{2}\rho C_D C_f \alpha_{eq} V_{eq}^2 S_w \qquad (74)$$

$$L_w = \frac{1}{2}\rho C_L C_f \alpha_{eq} V_{eq}^2 S_w \qquad (75)$$

3.1.5. Controllers. The last objective of this study before simulations were completed was to lay out several controller design methods, and apply each method to the flapping wing aircraft system. The simulation results with each controller were then examined to determine the feasibility of each controller approach for future use in this project. Note that the system used in this part of the study was for the flapping wing aircraft with a tail, and that all controlled simulations were for two dimensional flights in the xz-plane. Since flight was restricted to a two dimensional plane, state equations for y, ψ, φ, v_y, ω_x, and ω_z could be neglected and their values in other equations could be set to 0. The state equation for x could also be neglected since for this first pass at controller

design no tracking was to be required for *x*, and also since no other controlled state equations include arguments of *x*.

The possible control signals for two-dimensional flight are the flapping frequency, *f*, and the nominal pitch angle of the wing, α_0. These two parameters are control signals because control of other system states is done by directly varying these values. The phrase "controller design" actually refers to determining the equation used to calculate the control signal in order that the states behave appropriately. In order to further reduce the complexity of the controller design, and because it is hard to visualize a varying frequency, *f* was assumed constant for these simulations. Terms without the α_0 can be lumped together to simplify the equations further, as in Equations 76 and 77. Therefore, the state equations for controller analysis were reduced to Equation 78.

$$F_{xt} = D_t \cos(\alpha_t + \alpha) - L_t \sin(\alpha_t + \alpha) \tag{76}$$

$$F_{zt} = L_t \cos(\alpha_t + \alpha) + D_t \sin(\alpha_t + \alpha) \tag{77}$$

$$\begin{bmatrix} \dot{z} \\ \dot{\theta} \\ \dot{v}_x \\ \dot{v}_z \\ \dot{\omega}_y \end{bmatrix} = \begin{bmatrix} -s_\theta v_x + c_\theta v_z \\ \omega_y \\ \frac{1}{m}\left(D_w c_\beta + L_w s_\beta + F_{xt}\right) - \omega_y v_z - g s_\theta \\ \frac{1}{m}\left(L_w c_\beta - D_w s_\beta + F_{zt}\right) + \omega_y v_x + g c_\theta \\ \frac{1}{I'_{yy} m}\left\{\left(L_w c_\beta - D_w s_\beta\right)X_w - F_{zt}X_t\right\} \end{bmatrix} \tag{78}$$

3.1.5.1. Output Tracking via Feedback Linearization. The first controller was designed via feedback linearization of the output. The output in this instance was the altitude; therefore $y_{out} = z$, and it was desired to make this output track a reference z_{ref}.

Notice though, that z is not an expression which contains the control term, α_0. Therefore,

z was differentiated until α_0 appeared.

$$\dot{y}_{out} = \dot{z} = -s_\theta v_x + c_\theta v_z$$

$$\ddot{y}_{out} = \ddot{z} = -(c_\theta v_x + s_\theta v_z)\omega_y - s_\theta \dot{v}_x + c_\theta \dot{v}_z$$

$$= \frac{\rho S_w}{2m}\left[-s_\theta(C_L s_\beta + C_D c_\beta) + c_\theta(C_L c_\beta - C_D s_\beta)\right]C_f \alpha_{eq} V_{eq}^2 + c_\theta F_{zt} - s_\theta F_{xt} + g$$

$$\ddot{y}_{out} = \ddot{z} = \frac{\rho S_w}{2m}\left[C_L \cos(\beta + \theta) - C_D \sin(\beta + \theta)\right]C_f \alpha_{eq} V_{eq}^2 + c_\theta F_{zt} - s_\theta F_{xt} + g \quad (79)$$

Next, in order to control the system error between the output and its reference, Equation

80 was developed by letting

$$\ddot{z} = \ddot{z}_r - k_1 e - k_2 \dot{e} \quad (80)$$

Rearranging Equation 80 created the system error dynamic equation, where $e = z - z_{ref}$,

$\dot{e} = \dot{z} - \dot{z}_{ref}$, and $\ddot{e} = \ddot{z} - \ddot{z}_{ref}$.

$$\ddot{e} + k_2 \dot{e} + k_1 e = 0 \quad (81)$$

With Equation 81, the error dynamics were set by selecting values for k_1 and k_2.

Once the error dynamics were acceptable, Equation 80 was equated with Equation 79,

and with Equation 68, the necessary control signal was found.

$$\alpha_0 = \frac{\ddot{z}_{ref} - k_1\left(z - z_{ref}\right) - k_2\left(-s_\theta v_x + c_\theta v_z - \dot{z}_{ref}\right) + s_\theta F_{xt} - c_\theta F_{zt} - g}{\frac{\rho S_w}{2m}\left[C_L \cos(\beta + \theta) - C_D \sin(\beta + \theta)\right]C_f V_{eq}^2} + \beta \qquad (82)$$

3.1.5.2. Controller Design with Lyapunov Function. The Lyapunov approach [20] to controller design uses a positive definite function to approximate the system energy. The selection of the positive definite function is more or less arbitrary, but it can be quite difficult to select a function that performs correctly. The Lyapunov function, V, of the system states, $\mathbf{x}$, must be positive definite, that is as

$$\|\mathbf{x}\| \to \infty \quad \text{then} \quad V(\mathbf{x}) \to \infty$$

Using this approach, any state used in the Lyapunov function will be regulated; that is, the state should be driven to 0. Since some states, like v_x, should not be zero in steady-level flight, an error-state should be developed for these states or they should be omitted from the Lyapunov function. In this case, the Lyapunov function was selected to regulate an error-state for the altitude, z, and the pitch rate, ω_y. The error-state is very simple to develop when a constant reference is desired, because the derivative of the reference is 0. The Lyapunov function used for this study is in Equation 84.

$$z_e = z - z_{ref}$$

$$\dot{z}_e = \dot{z} - \dot{z}_{ref} = -s_\theta v_x + c_\theta v_z \qquad (83)$$

$$V = \frac{1}{2}z_e^2 + \frac{1}{2}\omega_y^2 \qquad (84)$$

To ensure system stability, the time derivative of V should be negative definite. In other words

$$\dot{V}(\mathbf{x}) \to -\infty \quad \text{as} \quad \|\mathbf{x}\| \to \infty$$

The above statement means that as the states proceed away from their equilibrium point, the derivative of the energy function becomes more negative. Hence, if V represents some form of the energy of the system, then the energy is always decreasing until the system is in equilibrium. Therefore, this method of Lyapunov design is to calculate a control signal such that $\dot{V}$ is negative definite. The exact form of $\dot{V}$ after the control signal is calculated will determine the method of convergence of the states. In this case, it was desirable that

$$\dot{V} = -z_e^2 - \omega_y^2 \tag{85}$$

This form of the Lyapunov derivative indicates global asymptotic stability; that is, for any initial conditions, if the Lyapunov derivative is of this form, the states will return to their equilibrium point, which in this case would be $\begin{bmatrix} z_e & \omega_y \end{bmatrix}_{eq}^T = \begin{bmatrix} 0 & 0 \end{bmatrix}^T$.

Proceeding, the time derivative of Equation 84 was

$$\dot{V} = z_e \dot{z}_e + \omega_y \dot{\omega}_y = z_e \left(-s_\theta v_x + c_\theta v_z \right) + \omega_y \frac{\rho S_w}{2mI_{yy}'} \left[\left(C_L c_\beta - C_D s_\beta \right) C_f \alpha_{eq} V_{eq}^2 X_w - F_{zt} X_t \right]$$

$$\tag{86}$$

With early uncontrolled simulations, ω_y was well behaved and very stable, so it may have been a little confusing at the beginning of this section why this state would need to be regulated. Upon examination of Equation 86 though, it is obvious that a state besides z_e must be introduced for regulation in this approach since the state equation for z_e does not contain any control terms to be solved for. The reason v_x or v_z was not used was because error-states would have to be developed for them, and the exact references were not know. ω_y is a much stronger state to use also, because regulation of ω_y should mean that the aircraft is flying at a constant angle. Setting Equation 85 and 86 equal, the control signal was found as

$$\alpha_0 = \frac{2mI_{yy}'\left\{z_e\left(s_\theta v_x - c_\theta v_z\right) - z_e^2 - \omega_y^2\right\} + \rho S_w F_{zt} X_t \omega_y}{\rho S_w \left(C_L c_\beta - C_D s_\beta\right) C_f V_{eq}^2 X_w \omega_y} + \beta \qquad (87)$$

3.1.5.3. Optimal Control via State Dependent Riccati Equation. Optimal control uses a cost function to find the optimal trajectory required to regulate the states. The cost function in Equation 88 is a general equation used in optimal control, where Q and R are user selected matrices.

$$J(u) = \int_0^\infty \left(\mathbf{x}^T Q \mathbf{x} + \mathbf{u}^T R \mathbf{u}\right) dt \qquad (88)$$

Q and R help the designer weigh the states or the control signal. For example, if the states must perform with high precision and it is of no consequence how the control signal behaves, Q would be very large and R would be relatively small in comparison.

On the other hand, if control is at a premium and the state error is of no importance, R would be very large and Q would be small. In this study, the latter example is the case, since $\alpha_0 \leq \dfrac{\pi}{2}$.

The Riccati equation in Equation 89 is solved for S, where S is used to calculate the control signal in Equation 90 that minimizes the cost function in Equation 88.

$$A^T S + SA - SBR^{-1}B^T S + Q = 0 \qquad (89)$$

$$\mathbf{u} = -R^{-1}B^T S\mathbf{x} = -K\mathbf{x} \qquad (90)$$

A and B are the system matrices composed of the coefficients of the states and control signal respectively. However, since this system is nonlinear, the states and control signal are multiplied by other states. This leads to the State Dependent Riccati Equation (SDRE) [21]. When using the SDRE, the system is put in a pseudo linear form; a single state is factored out of each term and the remaining term is evaluated at that specific time step to produce a coefficient. In other words,

$$\dot{\mathbf{x}} = A(\mathbf{x})\mathbf{x} + B(\mathbf{x})\mathbf{u} \qquad (91)$$

$A(\mathbf{x})$ and $B(\mathbf{x})$ are attached in the Appendix. Notice in $A(\mathbf{x})$ that the v_f^2 term was divided by v_x in the v_x column of the matrix. This forced the v_f^2 term to be pseudo linear since no state could be factored out of the term in its original form by using the approach

$$v_f^2 = v_f^2 \frac{v_x}{v_x} = \frac{v_f^2}{v_x} v_x$$

This method lets the v_f^2 term become a coefficient of v_x. After the system matrices were

developed, Q and R were selected for input to the built-in Matlab command

$$[K, S, eig] = lqr(A, B, Q, R) \qquad (92)$$

This command returns the controller gain K in Equation 90. S is the solution of the

Riccati equation, and *eig* are the eigenvalues of the system. Note that since this is a

SDRE, Equation 92 is evaluated at every time step during simulations and as such, K, S,

and *eig* change with every time step.

  3.1.5.4. State Dependent Regulator. The system was placed in pseudo linear

form for the State Dependent Regulator exactly in the same way as for the SDRE.

Therefore, the A and B matrices in the Appendix apply to this controller as well. With

this approach however, system eigenvalues are selected such that they remain constant

for every time step. The control signal gain must still be calculated at every time step

with

$$G = acker(A, B, [p_1\ p_2\ p_3\ p_4\ p_5]); \qquad (93)$$

G represents the one by five gain vector that took the place of K in Equation 90.

p_1-p_5 were the desired system eigenvalues to be placed by the *acker* command. The *place*

command could have been used in this method; however the *acker* command can place

complex conjugate poles while the *place* command cannot.

3.2. RESULTS

3.2.1. Simulations. The fixed wing aircraft simulations performed quite well; or

as well as can be expected for a first time aircraft designer. When the small angle of

attack theory used for stability analysis was used in simulations (ie. $F_z = L$ and $F_x = D$)

along with arbitrary values for T, α_w, and α_t, the aircraft responded with a either a

climbing or falling parabolic flight path. Steady-level flight was also obtained with a

calculated constant thrust value during simulations. However, using the vertical and

horizontal forces developed with components of lift and drag produced drastically

different results, as seen in Figure 3.10.

Although the aircraft was still stable, the flight path was a series of loops. The

steady level flight simulations were also significantly different from the small angle

theory simulations, but this was because of the inability of Matlab to solve Equation 55

due to optimality constraints in the built-in Matlab command *fsolve.*
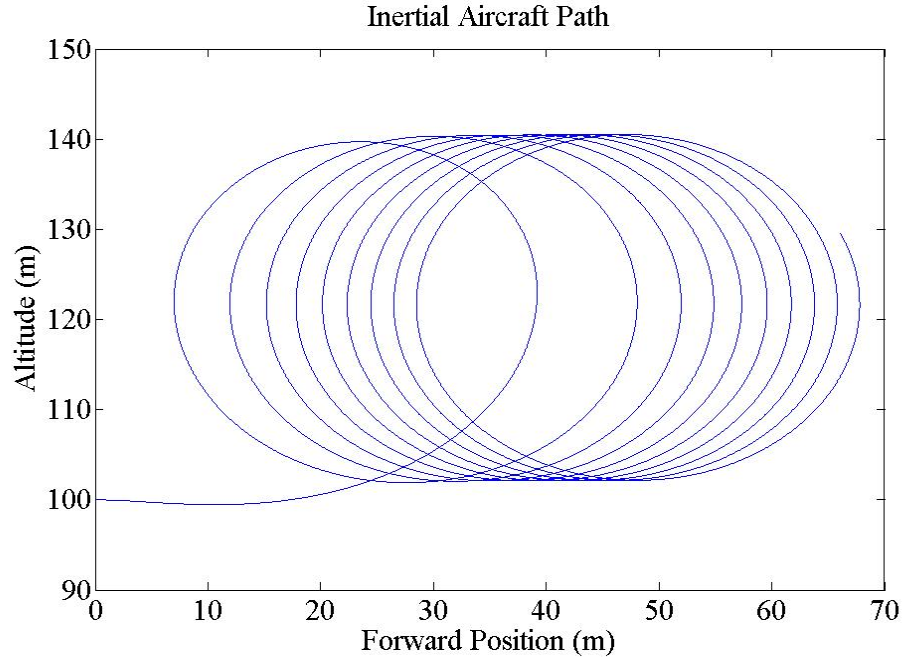
Figure 3.10. Aircraft Path, x vs. –z, for Fixed Wing Aircraft with Vector Forces.

Simulations for the flapping wing aircraft were extremely more difficult. Without precedence of dynamic simulations for a flapping wing model using this empirical approach, not much was known about exactly how the aircraft should behave for a given set of inputs. Adding to the difficulty is the selection of the three simulation inputs, α_0, α_t, and f. Again, a base value of these parameters was not available, and so selections at first were hit and miss. However, two of these parameters could be estimated, or at least bounded, with a fair amount of certainty. For α_t, it was clear after flight tests with the models purchased from [19] that a negative tail incidence angle was desirable for level or climbing flapping wing flight. Also, it was assumed that a flapping frequency much greater than 20 *Hz* could not be realized at this scale due to mechanical and structural limitations. As for α_0, too high of an angle here would not produce much lift, but too

small of an angle would just produce close to zero net lift throughout the stroke, and very little thrust. Nevertheless, α_0, could still be bounded by $\dfrac{\pi}{2}$.

Early simulations repeatedly showed singularities in the calculations. If the aircraft went into too steep of a dive or climb, an infinite derivative stopped all calculations immediately. However, some simulations seemed to be headed in the right direction early on, because even though α seemed unstable, the aircraft flight at times was reasonable. This was chiefly due to two main model errors. First, since no stall model was incorporated in the aircraft dynamics, an increasing angle of attack inevitably resulted in increasing lift (or drag). While it is [15] indicates that flapping wings usually operate at higher angles of attack, it is doubtful that this includes angles on the order of 90°.

Also, the tangent function used to calculate the angle of attack in Equation 68 was implemented in Matlab as an *atan* function which only considers angles in the first and fourth quadrants. So, every time the angle of attack would reach 90°, for example, a discontinuity would occur such that the angle of attack at the next time step was -90°. If these two errors had not been noticed, the model would have seemed stable.

Eventually, these and other problems were found and corrected. The final model responded quite well during simulations. In Figure 3.11, the altitude and aircraft angle of attack versus time can be seen. For Figures 3.11 and 3.12, the initial conditions for the states, $\mathbf{x}$ were $\mathbf{x}(0) = [0,0,-100,0,\pi,0,-15,0,0,0,0,0]^T$.
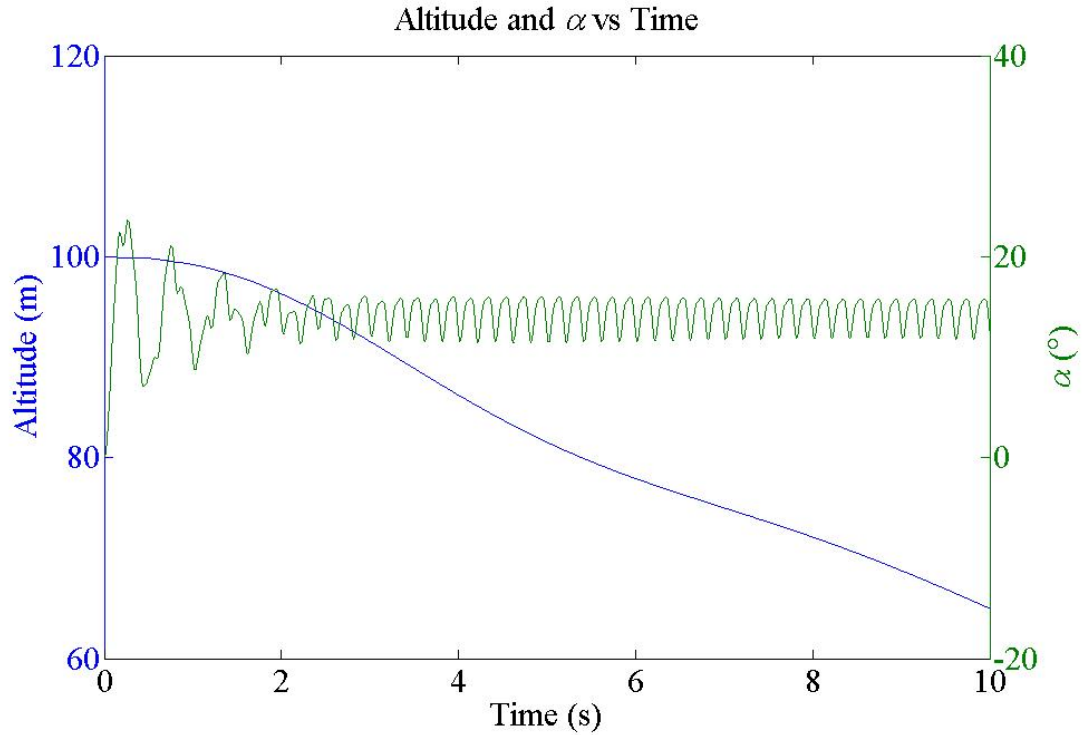
Figure 3.11. Altitude and α Versus Time with $f = 5$ *Hz*, $\alpha_0 = 10°$, $\alpha_t = -10°$.

Notice that $\theta = \pi$ was used to rotate the inertial frame into the desired body frame position, which also explains the negative signs for the altitude and v_x. As such, this angle for θ was always used as the "starting point". These two parameters must always be negative; if the altitude was positive, then the aircraft has hit the ground, and if v_x was positive, the aircraft was flying backwards. The input parameters for each simulation are provided with the figures. It was also found that the steady state oscillation frequency of the states is very close, in fact almost identical, to the input flapping frequency. This could be of use in future studies if a linearization technique is attempted, because although it was suspected that the state outputs would be oscillatory in nature, it was not known what this oscillation frequency would be. In linear systems theory, the output should have the same frequency as the input, but here, the coefficient

derivatives are twice the input frequency, and therefore it was thought that the output

frequency could possibly be 2f.
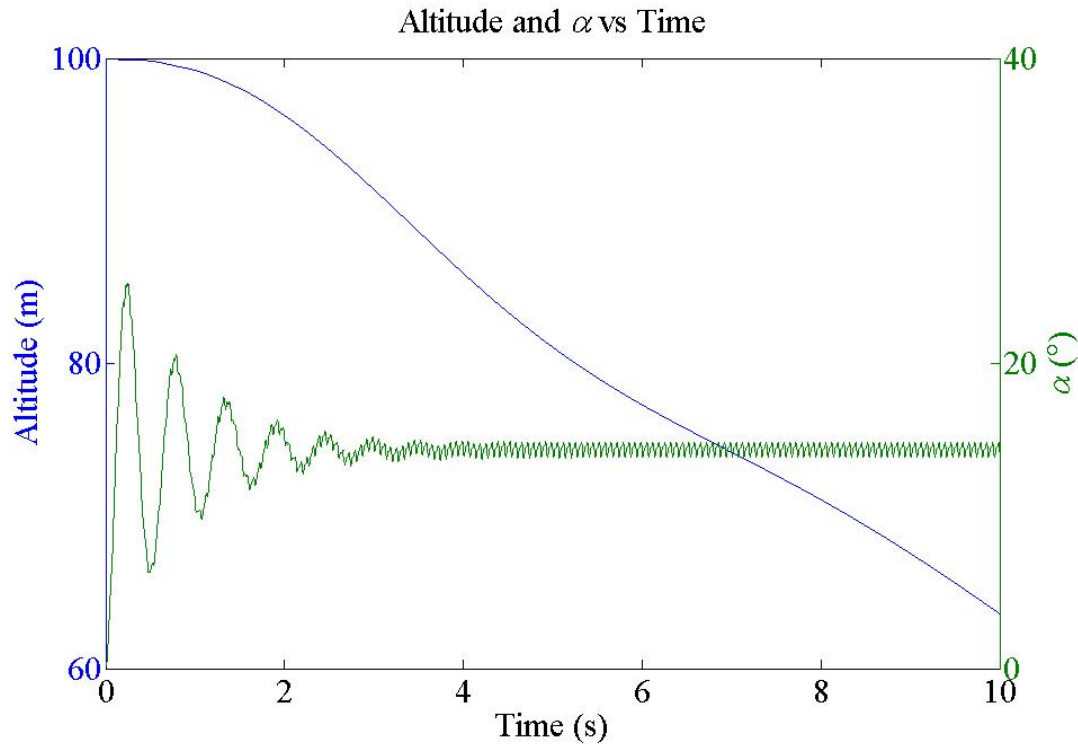
Figure 3.12. Altitude and α Versus Time with f = 15 Hz, α_0 = 10°, α_t = -10°.

Examining the two figures, it is evident that the amplitude of the steady state

oscillations is much smaller in Figure 3.12 than in Figure 3.11. Also notice that the angle

of attack does not settle on 0°, but on approximately 18°. This was due to the tail

incidence angle discussed earlier, and also to the variation of the pitch angle, α_0, in the

wing stroke. Even though a similar response with respect to angle of attack behavior

could be produced for an aircraft with a positive tail incidence angle, the positive angle of

the tail surface causes the aircraft to nose down; hence the aircraft hit the ground within 3

- 4 seconds. Using flapping frequencies on the order of 20 Hz, climbing flight could

never be produced. Consequently, the magnitude of the flapping frequency and tail

incidence angle were increased in the hopes of finding steady-level flight conditions, and the result can be seen in Figure 3.13.
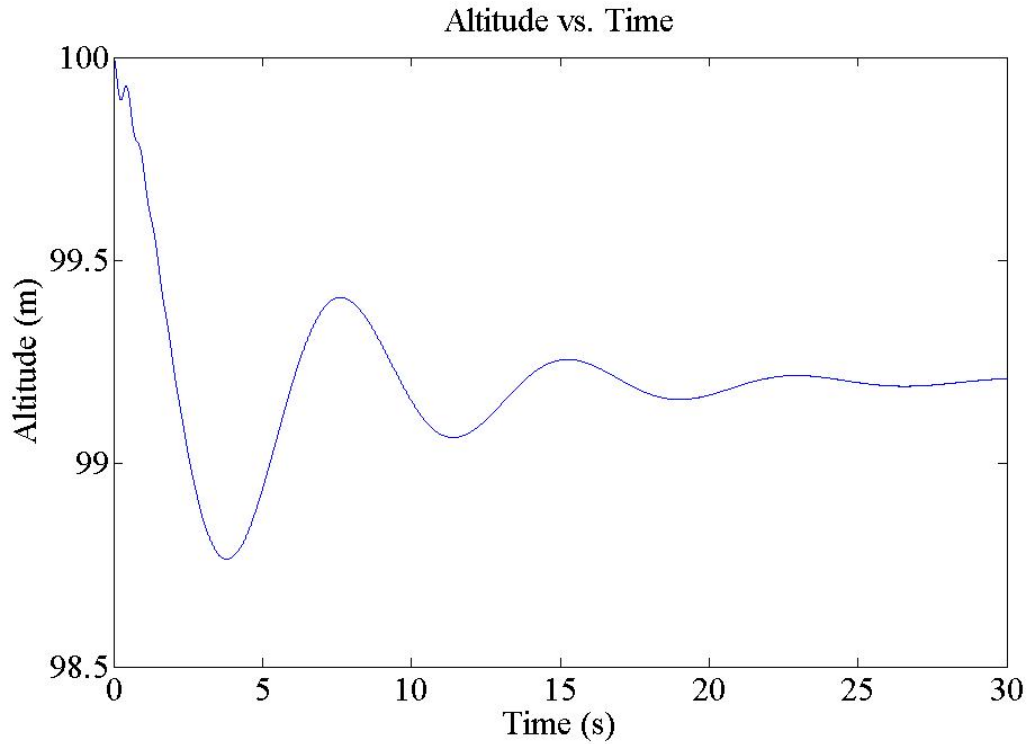
Figure 3.13. Altitude Versus Time with f = 116.325 Hz, α_0 = 4°, α_t = -9°.

In Figure 3.13 the aircraft was still slightly climbing at the end of the simulation, but when the state values towards the end of the simulation are substituted as initial conditions, the aircraft only climbs 0.035 m in a 30 second run time in Figure 3.14. The initial conditions for Figure 3.14 were $v_x(0)$ = -15.94 m/s, $v_z(0)$ = -3.6 m/s, $\omega_y(0)$ = 0.0305 rad/s, and $\theta(0)$ = 192.8° and these are referred to as the steady-level conditions or values throughout the rest of this paper. However, the flapping frequency used here is much too large to be realized with current equipment.
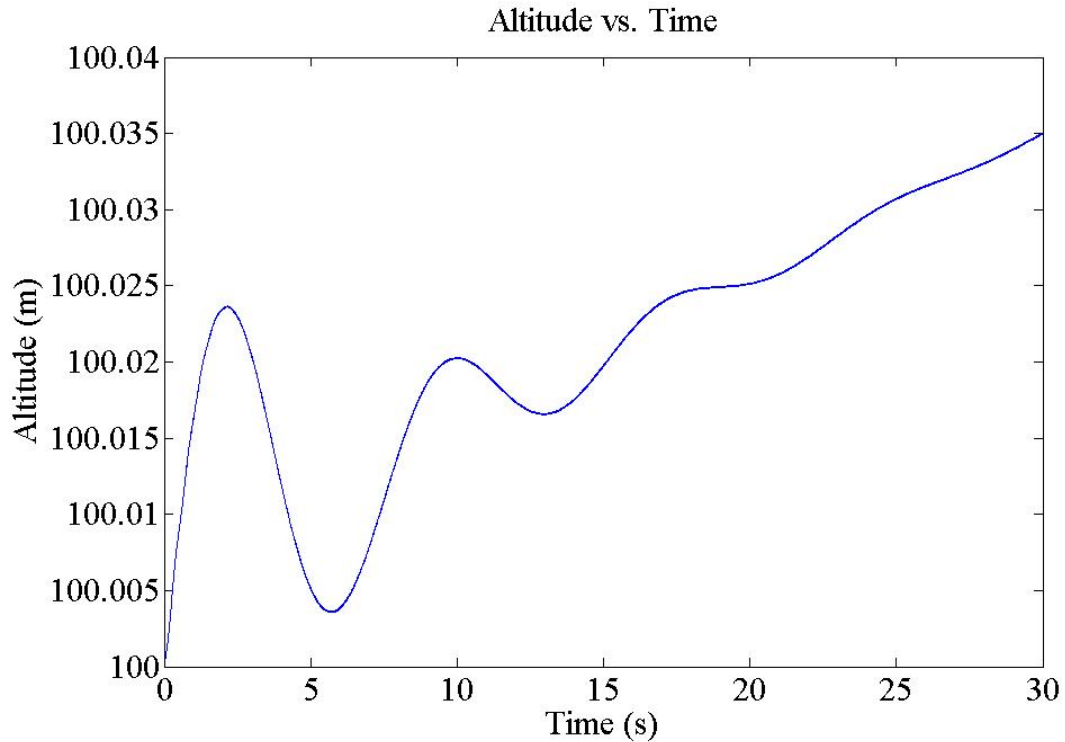
Figure 3.14. Altitude Response with Steady-State Values as Initial Conditions.

The power required for steady-level flight was calculated by multiplying the vertical force on the wing by the flapping velocity, v_f. The force in the horizontal direction was neglected since by definition, $P = F \bullet v$. Therefore, since velocity component in the direction of the horizontal force was ideally 0, the only remaining power came from the vertical force. Using this approach, the maximum power required at the wings is 1.65 W. This is a significant amount of power for such a small vehicle and is chiefly due to the high flapping frequency.

After a second look at Figure 3.6, it became a little clearer why such a high flapping frequency is needed for climbing or steady flight. Notice from Figure 3.6 that the force returns to zero at every extreme (or close to the extreme) of the stroke. After fitting a sinusoidal function and multiplying by a trigonometric function of the angle of attack, and dividing by a dynamic pressure using a constant velocity, the lift or drag

function still possesses the feature of returning to zero. The remaining manipulations to develop the coefficient derivatives do not change this fact either. So, at certain times during the flapping process, the forces acting on the flapping wing become zero, regardless of the flight conditions.

This cannot be correct though, because the body velocities will create some kind of force on the wings even if the wings were not flapping. The problem arises partly from using a constant velocity to develop the lift and drag functions. If the exact velocity at each time step was used, the lift and drag forces would be more exact, but another problem would arise; dividing by zero when the wing changes direction. Since a simple four-bar mechanism was used to drive the wing in the experiment, the velocity profile is a perfect sinusoid. Therefore, when a sinusoid was fit to the force function with the same frequency, both the velocity and force became zero at the same point. According to l'Hospital's Rule, if $\lim_{x \to a} f(x)$ and $\lim_{x \to a} g(x)$ equal 0 or $\pm \infty$,

$$\lim_{x \to a} \frac{f(x)}{g(x)} = \lim_{x \to a} \frac{f'(x)}{g'(x)} = \lim_{x \to a} \frac{f''(x)}{g''(x)} = \dots$$

Using this correlation, a nonzero quotient could be found. The end results were constant lift and drag functions; exactly like a fixed wing coefficient derivative.

So, using the above method, the unsteady effects embedded in the data are neglected by fitting a perfect sinusoid to the force data. In fact, when Figure 3.6 is examined closely, it can be seen that the points where the force is zero are out of phase with the data flapping frequency. This is because the wing was reversing direction at this

point and because of the unsteady effects associated with a flapping wing, the force will

not be zero exactly when the wing reversed direction. For instance, when the wing is

moving up just before the end of the stroke, it is "pulling" some fluid with it. When the

wing stops to reverse direction at the stroke extreme, the fluid's momentum continues to

push up on the wing and create a force. Therefore, the wing starts to move slightly in the

downward direction before the force becomes zero.

The lift and drag coefficient derivatives must then be calculated with the data at

each time step. Without analytical functions, l'Hospital's Rule cannot be used, but the

time step used while taking data could be set up in such a way that the velocity is never

exactly zero, and hence, the lift or drag would never be infinity. While the lift or drag

could still become a very large number when the velocity becomes close to zero, the

manipulation in Equation 62 would still work since it would be using a finite number.

Finally, a spline could be used to fit a more exact equation to the coefficient derivative so

the result could be used in simulations.

The three dimensional simulations did not perform well in the sense that no set of

conditions were ever found which resulted in steady level flight. However, to start the

simulations, α_L and α_R were set equal to each other to gauge the system response against

the flapping wing NAV with a tail and the tailless NAV was stable for most inputs, but

the states did not settle as quickly as a comparable simulation with the tailed version as

can be seen in Figure 3.15. It is believed that without the presence of the energy-

absorbing tail, the aircraft was more prone to drawn out oscillations. As such, negative

lift from the wings was sure to have a more pronounced effect on this aircraft. Upon

further consideration, it is hard to think of a biological flyer that does not have some

secondary surface for control. Birds of course have a tail, but even butterflies possess a smaller set of wings behind their first set of wings. Therefore, from these first results and considerations, it was doubtful that this aircraft could ever maintain steady level flight. The initial conditions used for the simulation in Figure 3.15 were the steady level conditions obtained earlier.
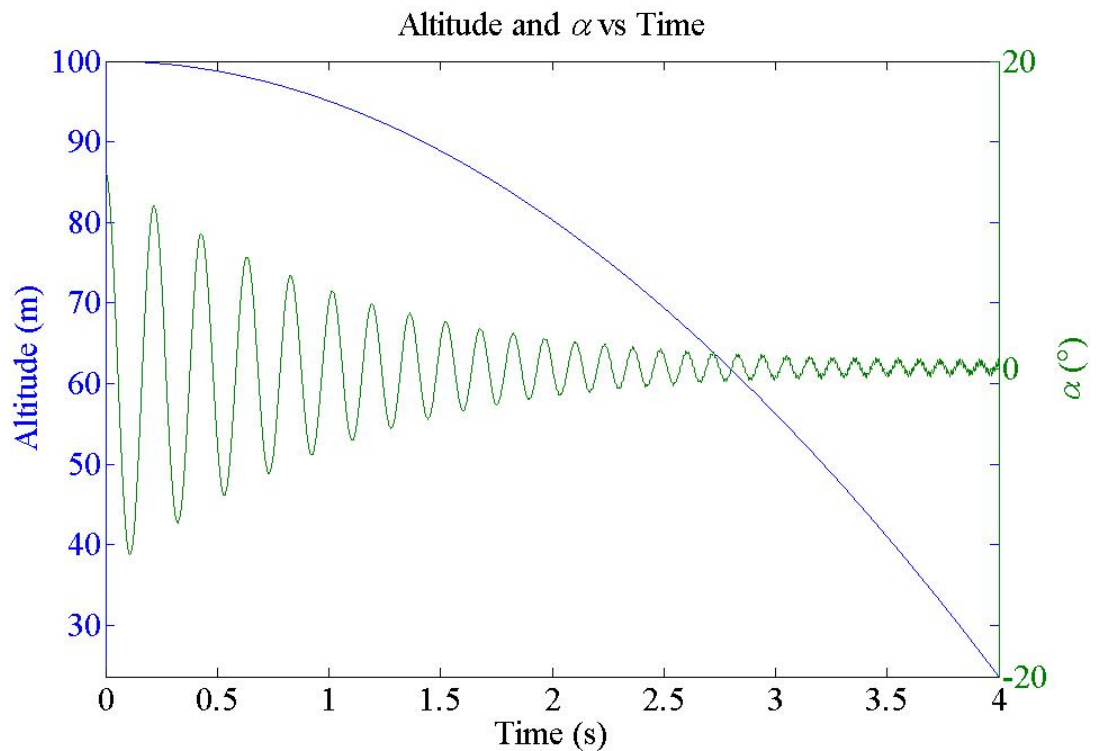
Figure 3.15. Two Dimensional Flight of Tailless NAV with $f = 80$ Hz, $\alpha_L = \alpha_R = 10°$.

However, another two dimensional simulation was attempted after considering how the variations in α_L and α_R were to be applied for three dimensional maneuvers. Assuming that the flapping mechanism would have a default nominal value for α_0, any changes, by a servo for example, would add to the pitch angle during one portion of the

stroke, and detract from the nominal angle during the reverse stroke. That led to a new

definition for α_0 with Equation 94.

$$\alpha_0 = s_n \alpha_{set} + \alpha_\delta \qquad (94)$$

In Equation 94, α_{set} represents the nominal pitch angle for each wing to follow. Any

variations in the angles between the wings are done through α_δ. This allows the

difference in the wings pitch angles to remain equal throughout the stroke, instead of one

wing angle being greater by some amount during the upstroke and then being less by that

amount during the down stroke.

Using this method, and letting $\alpha_{set} = 10°$ and $\alpha_\delta = 2°$, it can be seen in Figure 3.16

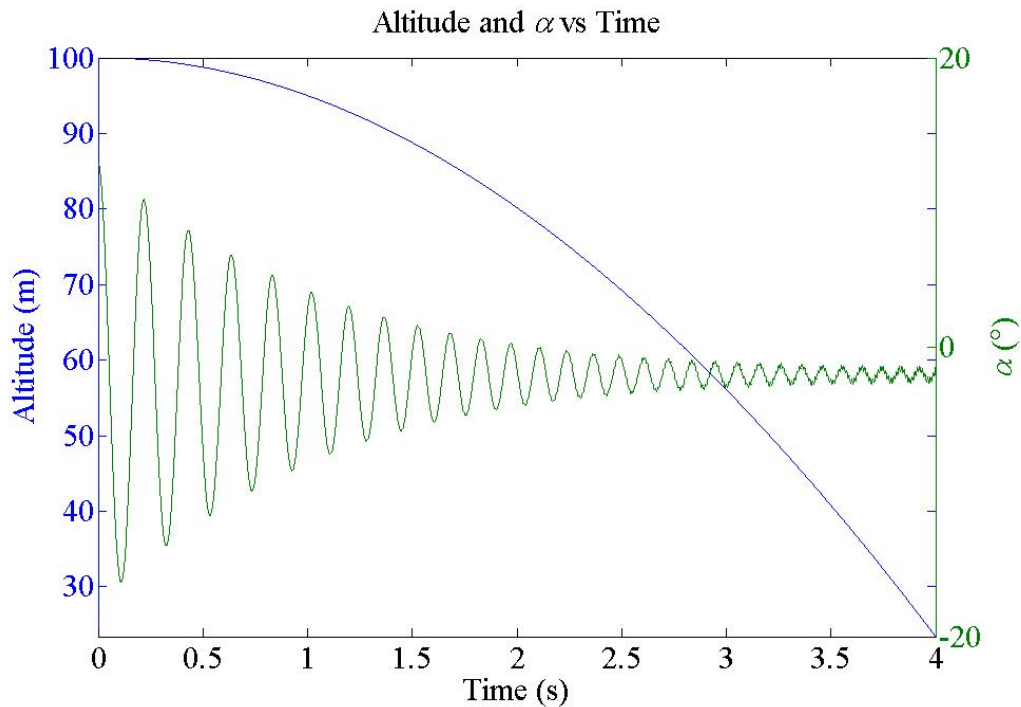that the aircraft does not fall quite as fast as in Figure 3.15.

Figure 3.16. Two Dimensional Simulation for Tailless NAV with Offset Pitch Angle.

Although the aircraft in Figure 3.16 still falls, this method could eventually be used to optimize the angle of attack when both wings are set at the same angle. By using a large α_{set}, and a large α_δ, there would be a larger positive angle during the upstroke and possibly a positive (or at least slightly negative) angle during the downstroke.

The three dimensional simulations for the tailless aircraft were not as favorable. During these simulations, the aircraft showed instability after a rotation had begun. Two approaches were used with these simulations; using an offset angle for the entire simulation and using an offset angle for just the first quarter second of the simulation. The second method was a feeble attempt to replicate a control signal; a quick correction to adjust flight. Figure 3.17 is a plot of the three dimensional flight path for a constant adjustment angle $\alpha_{\delta.L} = 2°$, while $\alpha_{\delta.R} = 0°$, $\alpha_{set.L} = 10°$, and $\alpha_{set.R} = 10°$.
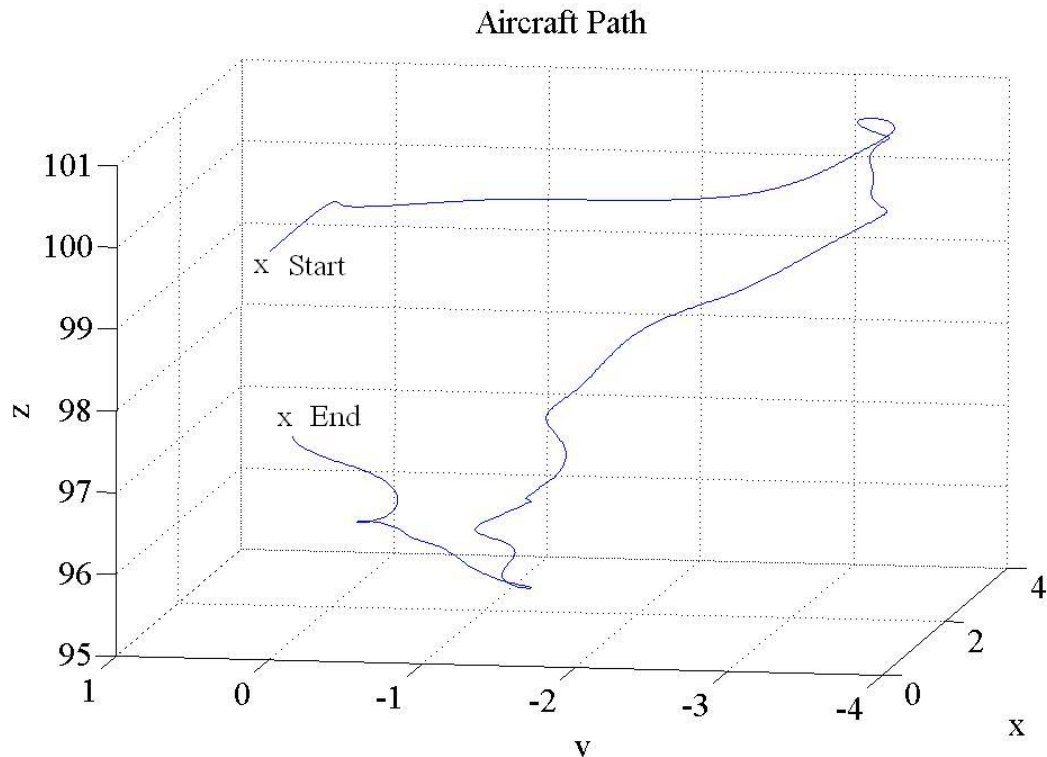
Figure 3.17. Three Dimensional Flight Path for Tailless NAV with $f = 80\ Hz$ and Offset Wing Pitch Angles.

Figure 3.17 presents another beacon of hope for the tailless aircraft. Once rotation began, the aircraft slowly climbed for a few meters, and then slowly it began to fall before climbing once again. Without an animation to show the exact orientation of the aircraft at all times, it is difficult to visualize how it accomplished these maneuvers, but after matching times between altitude and pitch angle plots, it was found that at some moments the aircraft was flying upside down while it was climbing.

The results from the impulse offset angle in Figure 3.18 look similar to Figure 3.17 initially, but once $\alpha_{\delta,L}$ is set back to $0°$, the aircraft continues to climb. Again, the pitch angle indicates that at times the aircraft is upside down.
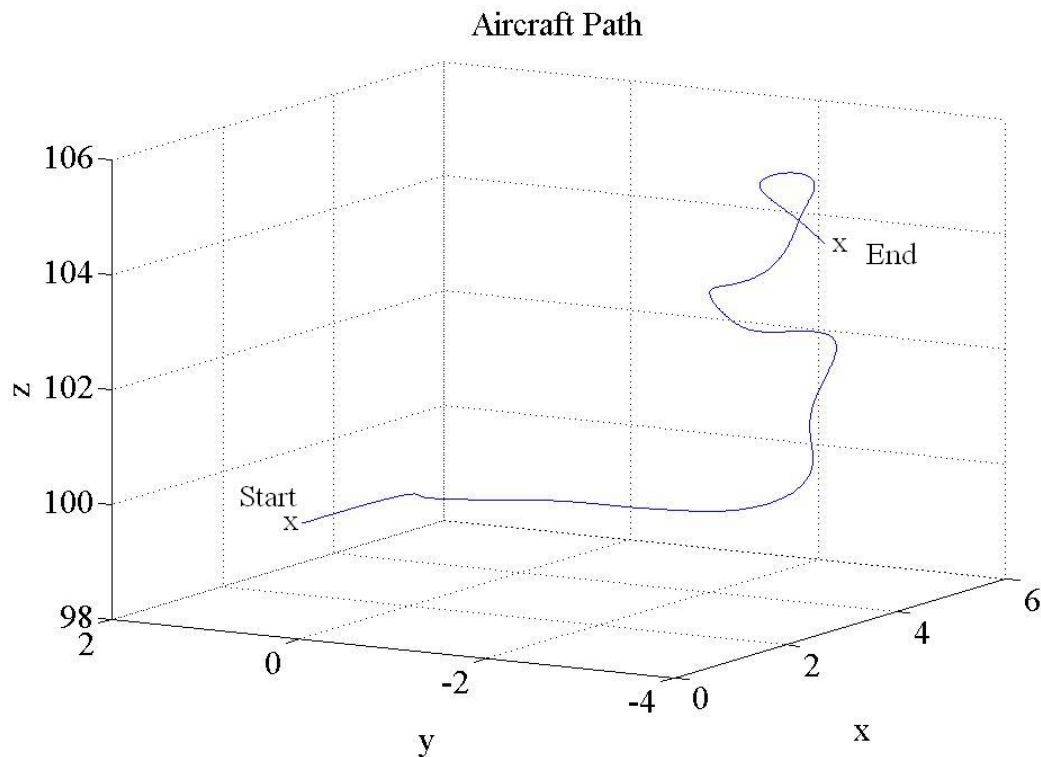

Figure 3.18. Three Dimensional Flight Path for Tailless NAV with $f = 80$ Hz and Momentarily Offset Wing Pitch Angles.

The fact that this aircraft experiences climb during moments when it is upside down, points to a number of problems. Mathematically, the aircraft may become more stable in this mode. This should not be the case due to the previous stability analysis. Secondly, perhaps not enough conditions were tried to achieve climbing flight when the pitch angles were not offset. Also, since the inertial terms were not canceled in the dynamic model for these simulations, they may add enough force to produce climbing flight whenever certain states have a non-zero value. Lastly, as is always a potential problem, there may be an error in the dynamic model, that was not encountered with previous simulations due to the cancellation of certain terms.

It is believed from these simulations that tailless flapping wing flight is possible, but difficult. At the very least, some sort of drag element should be placed in the rear of the vehicle to help keep the nose up.

3.2.2. Controller Simulations. All of the controllers designed previously failed to produce the desired results. In fact, most of the controllers drove the system unstable in a short amount of time. For a check point, the controller simulations were given initial conditions corresponding to the state values obtained during steady-level flight. The control signal should have followed closely to the input for the uncontrolled simulations. However, the control signal continued to grow throughout the controlled simulation until the system became unstable. In Figure 3.19, the altitude does not rise very quickly, but the fact that it does indeed climb indicates that the controller is not performing correctly.

Altitude and α vs Time
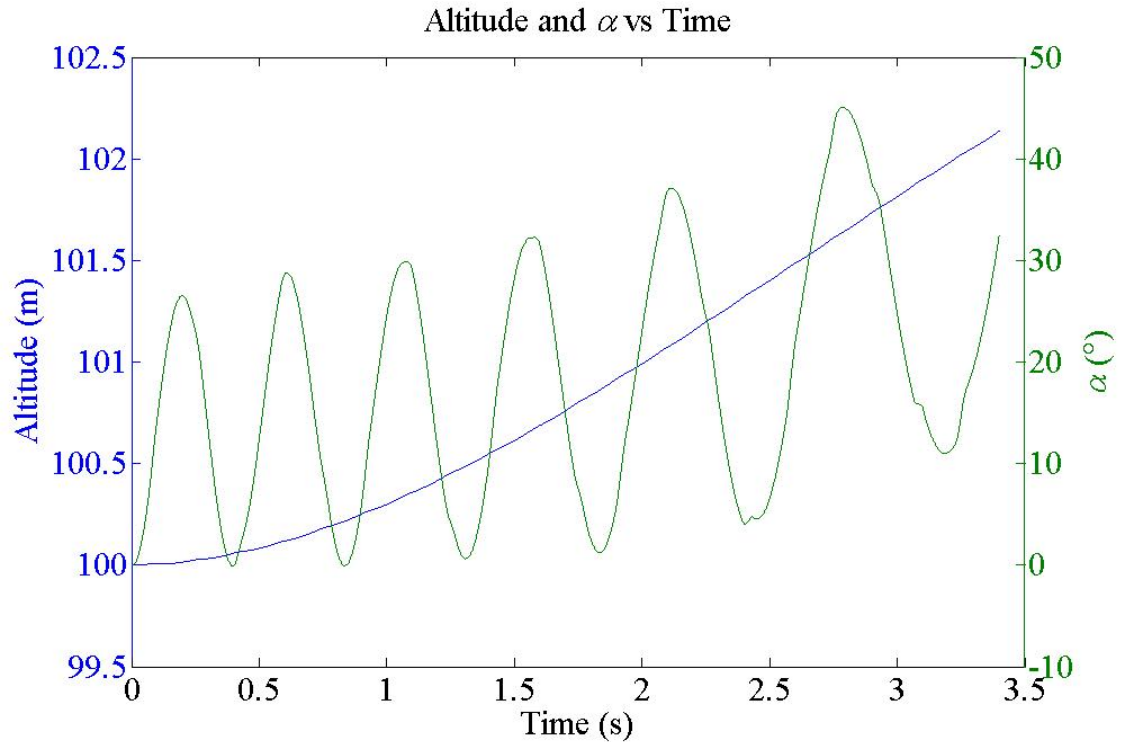
Figure 3.19. Altitude and α vs. Time with Feedback Linearization.

The angle of attack in Figure 3.19 also grows during the entire simulation. The gains k_1 and k_2 in the error dynamic equation were varied to examine the simulation results, but the feedback system is highly sensitive to these values. No set of conditions could be found to create a favorable response from the system. One positive detail to come from the feedback linearization analysis was the concept of step calculations. If Equation 82 were examined, it is clear that the control signal becomes infinite when $C_f =$ 0. Therefore, when C_f approaches zero, the calculations are canceled for a short time. Even though a saturation level can be set for the control signal, in a physical realization of this project, the actuator and the aircraft itself would not be able to respond to these changes in such a short amount of time.

The Lyaponuv simulations were even less optimistic, and with after examining Equation 87, it was clear why. In Equation 87, the numerator is divided by ω_y. So, if the controller is successful in regulating ω_y then α_0 becomes ∞. There is a "trick" when using Lyaponuv technique; since the derivative of V has to be less than zero and not equal to zero, terms are usually dropped, added, or manipulated in order to simplify the derivative. Although this approach was known, there were no apparent mathematical manipulations that would simplify the derivative.

The SDRE technique seemed most promising before simulations were started. It is a relatively easy method to apply, and changes to the system gains were as easy as making a new guess for Q and R. However, therein lies the problem for this method. The selection of the values for Q and R, other than an estimated knowledge of their relative size, is completely arbitrary. Many combinations of Q and R were attempted, but not one case was ever found that did not drive the system unstable, as seen in Figure 3.20.
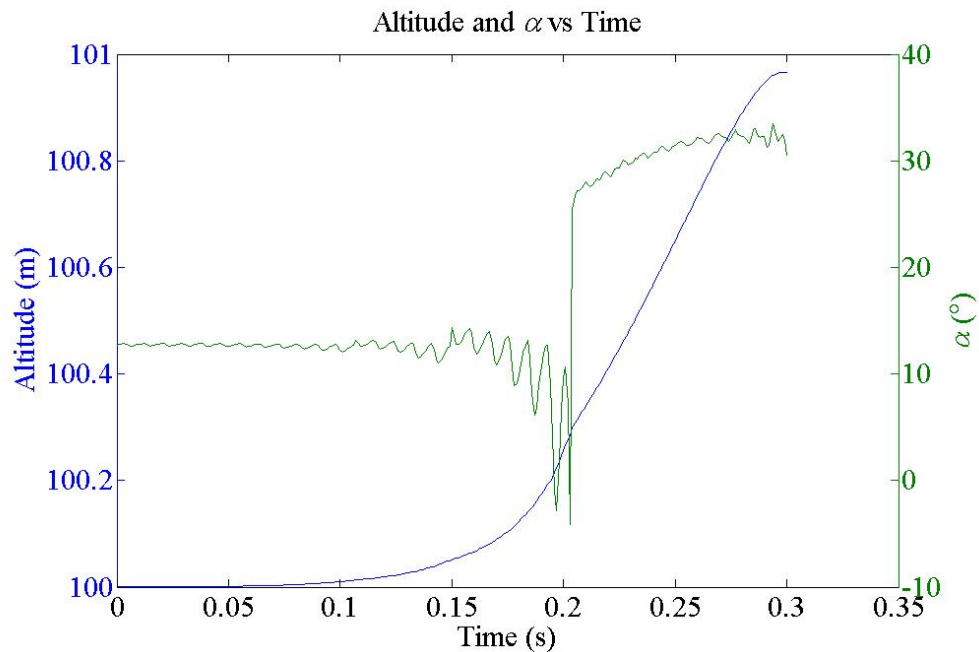
Figure 3.20. System Response with SDRE Control.

Notice that the simulation in Figure 3.20 ran for 0.3 seconds. This is because a

singularity or ill-conditioned *A* or *B* matrix arose after this time. This was typical of most

of the SDRE simulations.

The state dependent regulator had the best simulation results. This method was

still hit and miss, but that is true with almost all of these methods since so much depends

on the selection of poles or weight matrices or error dynamic constants. In Figure 3.21,

the angle of attack certainly becomes unstable, but the altitude is not responding correctly

at early in the run either. However, during this simulation, α_0 was at least feasible for the

entire run.

Figure 3.21. Altitude and α vs. Time for a State Dependent Regulator.

Refinements were made to these last two methods in a hope to regulate the

controller dynamics. Due to the discontinuity of s_n, the control signal undergoes highly

dynamical behavior. In fact, a physical actuator would not be able to realize the

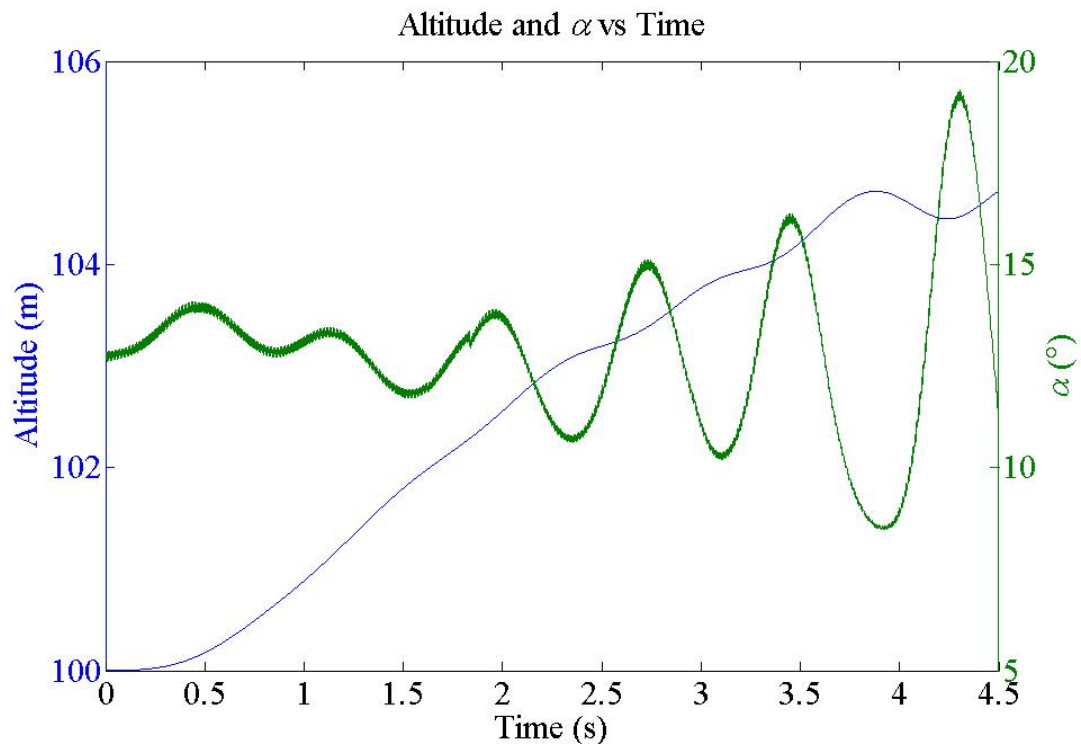dynamics induced in the control signal by the signum function. Recall from earlier

discussions that a constant velocity was used to calculate the coefficient derivatives, and

therefore this signum function is needed to present both signs of the velocity in the

calculations. The true sinusoidal velocity function calculated from the flapping

mechanism should help all of these simulations, but for now an integrator was applied to

the SDRE system. An integrator helps smooth out the control signal α_0, now a state,

since the linear quadratic regulator is trying to drive α_0 to zero. $\dot{z}$ was also added as a

state to try and smooth out the altitude path. Note that these two steps were only applied

to the SDRE system. The final SDRE results can be seen in Figure 3.22, while the state

dependent regulator changes are in Figure 3.23.
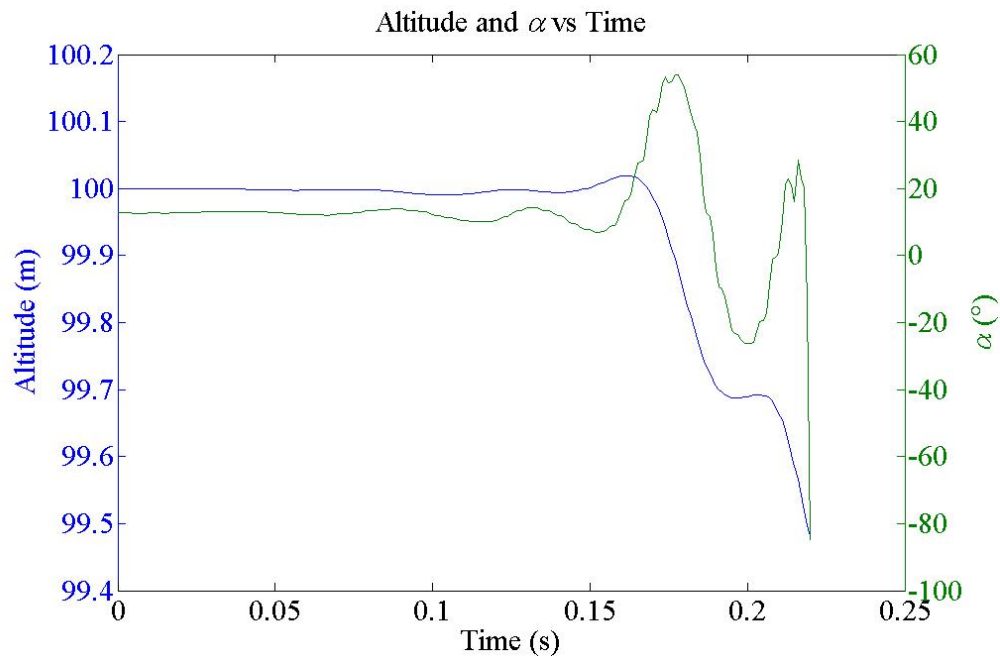
Figure 3.22. Altitude and α vs. Time for a SDRE with an Integrator and $\dot{z}$.
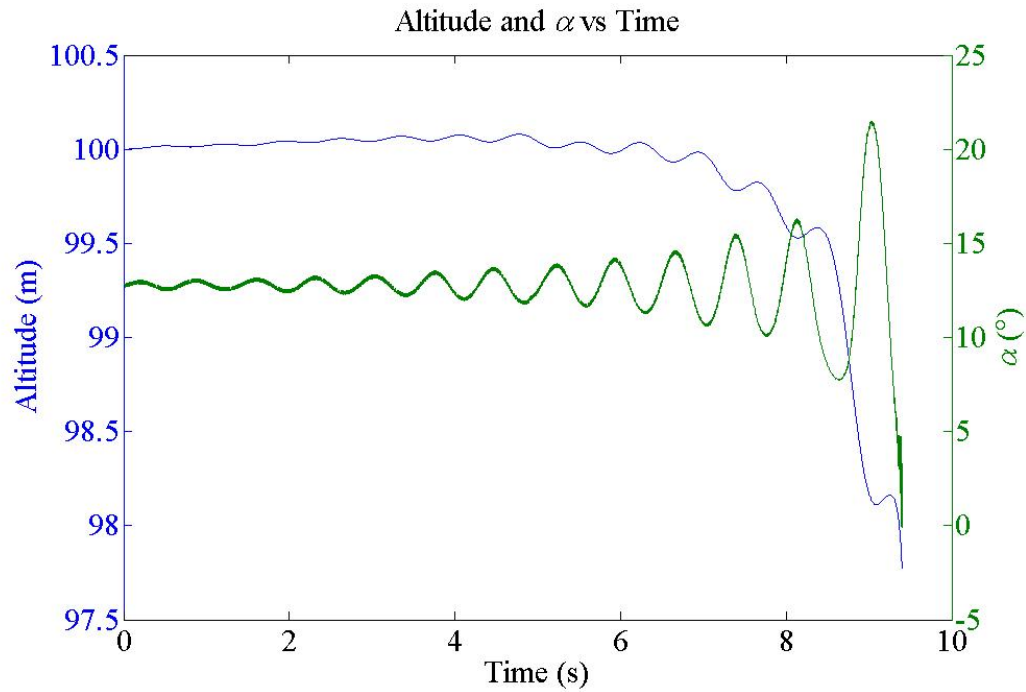
Figure 3.23. Altitude and α vs. Time for a State Dependent Regulator with Nominal
Control Signal.

A nominal control signal was added to both the SDRE and state dependent

regulator systems. This control signal is needed since during steady level flight, a non-

zero control signal is needed. The nominal control signal was obtained from the

uncontrolled steady level simulations.

As is seen in the figures, both systems seem to behave quite well at first.

However, the instability builds slowly to drive the system unstable. Notice the time scale

in Figure 3.22. Again, like simulations in Figure 3.20, the state dependent matrices used

in the Riccati equation become ill conditioned after a short time. The most promising

results from the controller analysis seem to point to the final arrangement of the state

dependent regulator.

4. CONCLUSION

This project was a great success in developing an approach for creating a statically stable flapping wing aircraft. Although a large number of cases were tried that resulted in an unstable system, the same can be said for a great deal of nonlinear systems; the positive point is that many combinations were found in which the aircraft was stable. As discussed earlier, it is doubtful that the coefficient derivatives would ever be zero if the velocity at each point in the stroke was used instead of an average velocity when the empirical lift and drag functions were calculated. That does not take away from the usefulness of this study however, since a plane that flies at moments when zero lift is present will sure fly when the lift is non-zero.

Although all of the control schemes failed to track the desired constant altitude reference in this study, they can still be used as a guideline for controller development later on in this project. It is quite possible that the controllers were trying to be too exact when regulating the system. In fact, when the calculated control signal of the SDRE system at the second time step was compared to the control signal used for steady level flight, the SDRE control was much higher. This points to the controller trying to drive out any oscillations from the states, but this is contradictory to the uncontrolled steady level simulations. It is evident that this system will have some oscillations during steady state flight, so some error will have to be accepted in the controller.

Since the system error can be weighted with SDRE control, this is the control method that is suggested for future work. The state dependent regulator would also be a good choice, since both of these methods are easy to implement and manipulate, but with

the SDRE it is simpler to select user inputs given that the selections of the Q and R matrix don't physically mean anything. With the state dependent regulator, the selection of the system poles (or eigenvalues) corresponds directly to the state responses. Another advantage of the SDRE control is that many other optimal control techniques can be applied later if the system is found to work with SDRE. After the three dimensional simulations, it is also suggested that any future considerations include a tail of some form. A tail of the length and shape used for this NAV is not necessarily needed; by simply decreasing L_f at the beginning of Section 3 the aircraft length can be diminished to further reduce weight, but a tail should be on the flapping wing aircraft to keep the nose up and help with other aspects of stability. Even a bulbous piece of balsa wood projected at an upward angle behind the aircraft could help keep the nose up…although the aerodynamics might be difficult to model.

It was stated in the simulation results that the power required by both wings during the steady level flight was 1.65 W. As few aircraft have actually been built at the NAV scale, it is hard to judge if this power requirement is the norm. However, based on the MAV in the literature review, this seems like a large value. Furthermore, this is only the power required at the wings; the actual motor power rating would have to be larger still due to losses in the motor and flapping mechanism, inaccurate assumptions in the force model, and power requirements by onboard computing and control equipment. Again, this power requirement is due to the extremely high flapping frequency, which would probably be lower with refinements to the experimental data.

The data from [15] was not originally developed for the purpose of creating these derivatives. The flapping velocity and force data were not taken simultaneously and

therefore, even though the exact data was available, it could not be assured that the velocity at a given moment corresponded to the actual force at that moment. Data taken in moving fluid would also improve these coefficients, as it is suspected that the ambient fluid produces some sort of parasite force on the wing irregardless of the wing flapping velocity. This is speculation, but force data from in a moving flow field should indicate the accuracy of this assumption.

Since flapping wing aerodynamics are based upon unsteady effects from the wing rotations, both flapping and pitching, a study into any empirical correlations for data with various rotational properties (both acceleration and velocity for flapping and pitching) could also be performed to improve the system coefficients. Of course, this would require a wide array of data taken a multiple wing beat frequencies, pitching velocities, and angles of attack, but the worst it could do was verify the current model of the wing forces.

There are a number of ways that this project could be further improved with future work. Once the final flapping mechanism is selected, the continuous analytical velocity function of the wing can be substituted into the calculation of α_{eq} instead of using the $s_n v_f$ term. With known actuator dynamics, a more precise model of the nominal pitch angle could also be developed. With these two quantities redefined, a great deal of the discontinuities or "jumpiness" of the response would probably be avoided. In fact, this could possibly improve the controller design in the study as well, since a great deal of nonlinear control theory assumes the use of continuous state equations.

The dynamic model could also be improved by quantifying a number of terms that were neglected in this study. Fuselage lift and drag, forces due to sideslip, damping,

and the inertial terms corresponding to the actual aircraft shape and its wings could be

modeled to enhance the system model.

APPENDIX

$$A(\mathbf{x}) = \begin{bmatrix} 0 & 0 & -s_\theta & -c_\theta & 0 \\[2mm] 0 & 0 & 0 & 0 & \omega_y \\[2mm] 0 & -g\dfrac{s_\theta}{\theta} & -\dfrac{\rho S_w \beta}{2m}\left(C_L s_\beta + C_D c_\beta\right)C_f\left(\dfrac{v_f^2}{v_x} + v_x\right) + \dfrac{F_{xt}}{V_\infty^2}v_x & \left\{-\dfrac{\rho S_w \beta}{2m}\left(C_L s_\beta + C_D c_\beta\right)C_f + \dfrac{F_{xt}}{V_\infty^2}\right\}v_z & -v_z \\[4mm] 0 & g\dfrac{c_\theta}{\theta} & -\dfrac{\rho S_w \beta}{2m}\left(C_L c_\beta - C_D s_\beta\right)C_f\left(\dfrac{v_f^2}{v_x} + v_x\right) + \dfrac{F_{zt}}{V_\infty^2}v_x & \left\{-\dfrac{\rho S_w \beta}{2m}\left(C_L c_\beta - C_D s_\beta\right)C_f + \dfrac{F_{zt}}{V_\infty^2}\right\}v_z & v_x \\[4mm] 0 & 0 & -\dfrac{1}{I_{yy}'}\left\{\dfrac{\rho S_w \beta X_w}{2m}\left(C_L c_\beta - C_D s_\beta\right)C_f\left(\dfrac{v_f^2}{v_x} + v_x\right) - \dfrac{X_t F_{zt}}{V_\infty^2}v_x\right\} & -\dfrac{1}{I_{yy}'}\left\{\dfrac{\rho S_w \beta X_w}{2m}\left(C_L c_\beta - C_D s_\beta\right)C_f - \dfrac{X_t F_{zt}}{V_\infty^2}\right\}v_z & 0 \end{bmatrix}$$

$$B(\mathbf{x}) = \frac{\rho S_w}{2m}C_f V_{eq}^2 \begin{bmatrix} 0 \\[1mm] 0 \\[1mm] C_L s_\beta + C_D c_\beta \\[1mm] C_L c_\beta - C_D s_\beta \\[1mm] \dfrac{X_w}{I_{yy}'}\left(C_L c_\beta - C_D s_\beta\right) \end{bmatrix}$$

REFERENCES

[1]   R. Michelson, "Update on Flapping Wing Micro Air Vehicle Research," *13th Bristol International RPV Conference*, Bristol, UK, 30 March-1 April, 1998.

[2]   T. Pornsin-Sirirak, Y. C. Tai, C. M. Ho, M. Keennon, "Microbat: A Palm-Sized Electrically Powered Ornithopter," *Proceedings of NASA/JPL Workshop on Biomorphic Robotics*, 2001.

[3]   http://robotics.eecs.berkeley.edu/~ronf/MFI/. Micro-Mechanical Flying Insect (MFI) Project, June 2006.

[4]   J. Grasmeyer and M. Keennon, "Development of the Black Widow Micro Air Vehicle," *39th AIAA Aerospace Sciences Meeting & Exhibit*. AIAA 2001-0127.

[5]   J. Kellogg, C. Bovais, J. Dahlburg, R. Foch, J. Gardner, D. Gordon, R. Hartley, B. Kamgar-Parsi, H. McFarlane, F. Pipitone, R. Ramamurti, A. Sciambi, W. Spears, D. Srull, C. Sullivan, "The NRL MITE Air Vehicle," *16th Bristol International Conference on Unmanned Air Vehicle Systems*, Bristol, UK, April, 2001.

[6]   H. Y. Wu, D. Sun, Z. Y. Zhou, S. S. Xiong, X. H. Wang, "Micro Air Vehicle: Architecture and Implementation," *Proceedings of IEEE International Conference of Robotics and Automation*, Taipei, Taiwan, September 14-19, 2003.

[7]   http://findarticles.com/p/articles/mi_qa3819/is_200309/ai_n9254579. First Fuel-Cell Flight, *posted in September, 2003 by Matt Keennon*, June 2006.

[8]   R. Kumar, "MAVs: A Brief Summary," *National Aerospace Laboratories*, Document No. PDEA0011, June 2000.

[9]   G. Torres and T. Mueller, "Micro Aerial Vehicle Development: Design, Components, Fabrication, and Flight-Testing," *Presented at the AUVSI Unmanned Systems 2000 Symposium and Exhibition*, Orlando, FL, July 11-13, 2000.

[10]   C. Patel, H. Arya, K. Sudhakar, "Design, Build, and Fly a Solar Powered Aircraft," *Indian Institute of Technology*, Bombay, India, June 2006.

[11]   F. Bohorquez, P. Samuel, J. Sirohi, D. Pines, L. Rudd, "Design, Analysis and Performance of a Rotary Wing MAV," *Journal of the American Helicopter Society*, 2003.

[12]   http://aero.stanford.edu/mesicopter. A. Kroo, "The Mesicopter: A Meso-Scale Flight Vehicle," *Phase I Final Report*, June 2006.

[13] R. Barrett, "Adaptive Aerostructures: Improving High Performance Subscale Military UAVs," *45th AIAA/ASME/ASCE/AHS/ASC Structures, Structural Dynamics and Materials Conference*, Palm Springs, Californica, 19-22 April, 2004.

[14] L. Lipera, J. Colbourne, M. Tischler, M. Mansur, M. Rotkowitz, P. Patangui, "The Micro Craft iSTAR Micro Air Vehicle: Control System Design and Testing," *Presented at the American Helicopter Society 57th Annual Forum*, Washington, DC, 9-11 May, 2001.

[15] K. M. Isaac, J. Rolwes, A. Colozza, "Unsteady Flow Features of a Flapping and Pitching Wing at Low Reynolds Number," *36th AIAA Fluid Dynamics Conference*, 5-8 June, 2006.

[16] D. P. Raymer, *Aircraft Design: A Conceptual Approach*, 3rd Ed., AIAA Educational Series, © 1999.

[17] J. B. Duipers, *Quaternions and Rotation Sequences: A Primer with Applications to Orbits, Aerospace, and Virtual Reality*, 5th Printing, Princeton University Press, Princeton, NJ, 2002.

[18] Z. A. Khan, S. K. Agrawal, "Modeling And Simulation of Flapping Wing Micro Air Vehicles," *Proceedings of IDETC/CIE' 2005, 2005 ASME International Design Engineering Technical Conferences*, Long Beach, California, USA, September 24-28, 2005.

[19] http://www.ornithopter.org/store/falcon.info.html, http://www.ornithopter.org/store/funbird.info.html, *The Ornithopter Zone*, January 2007.

[20] H. K. Khalil, *Nonlinear Systems*, 3rd Ed, Prentice-Hall, Inc., Upper Saddle River, NJ, 07458, 2002.

[21] A. Bogdanov and E. Wan, "SDRE Control with Nonlinear Feedforward Compensation for a Small Unmanned Helicopter," *2nd AIAA "Unmanned Unlimited" Systems, Technologies, and Operations*, San Diego, California, September 15-18, 2003.

VITA

Wyatt Emery Davenport was born on April 25, 1984 in Chillicothe, Missouri. He graduated Summa Cum Laude with a B.S. degree in Mechanical Engineering in May 2006 from the University of Missouri-Rolla, Rolla, Missouri. Going directly into graduate school, he received his M.S. degree in December 2007 from the University of Missouri-Rolla, Rolla, Missouri. He presented a portion of his research to the NASA-Missouri Space Grant Consortium in April 2007. Wyatt was inducted into Pi Tau Sigma in December 2004. He began his career with Continental Energy Services in Carrollton, Missouri in September 2007.